Evaluations of Single Walled Carbon Nanotubes Using Resonance Raman Spectroscopy

by

Victor W. Brar

Submitted to the Department of Physics
in partial fulfillment of the requirements for the degree of

Bachelor of Science in Physics

at the

MASSACHUSETTS INSTITUTE OF TECHNOLOGY

June 2004

Author .....
Department of Physics
June 4, 2004

Certified by .....
Mildred Dresselhaus
Institute Professor
Thesis Supervisor

Accepted by .....
David E. Pritchard
Thesis Coordinator

Evaluations of Single Walled Carbon Nanotubes Using Resonance Raman Spectroscopy

by

Victor W. Brar

Submitted to the Department of Physics
on June 4, 2004, in partial fulfillment of the
requirements for the degree of
Bachelor of Science in Physics

Abstract

This work reports the results of two studies which use resonance Raman scattering to evaluate the vibrational properties of single walled carbon nanotubes (SWNTs). In the first study, we report an evaluation of second-order combination and overtone modes in highly ordered pyrolytic graphite (HOPG), in SWNT bundles, and in isolated SWNTs. We found both dispersive and non-dispersive Raman bands in the range 1650–2100 cm^{-1}, and we show that the appearance and frequency vs. laser energy E_{laser} behavior of these features are in agreement with predictions from double resonance Raman theory. In the case of SWNTs, these second-order bands depend on the one-dimensional structure of SWNTs, and, at the single nanotube level, the spectra vary from tube to tube, depending on tube diameter and chirality, and on the energy of the van Hove singularity relative to E_{laser}. In the second study, we present a theoretical method of predicting, to within a linear constant β, the frequency shift in the Raman features of a SWNT material as the Fermi level is changed by depletion or addition of electrons. This constant is then evaluated for different Raman modes in SWNTs by comparing theoretical predictions to experimental observations by Corio *et al.* , where the Fermi level of SWNT bundles is raised by electrochemical doping and Raman spectra are collected *in situ.* It is determined that for the G-band of SWNTs, the dependence of frequency on Fermi energy is $\beta_G = 271\mathrm{cm}^{-1}$ per hole per C-atom for metallic SWNTs with $\mathrm{d}_t \simeq 1.25 \pm 0.20\mathrm{nm}$.

Thesis Supervisor: Mildred Dresselhaus
Title: Institute Professor

Acknowledgments

This thesis is a summary of much of the work I have done in Prof. Mildred Dresselhaus' group, which I have worked in as an undergraduate researcher during my whole undergraduate career at MIT. During that time period, a number of people in or involved with the group have played major roles in my life at MIT, and I will be forever indebted to them.

I would first like to thank Professor Ado Jorio for all the time and energy he committed to teaching me and motivating me during my first two years here. His patience, kindness and persistence were instrumental in giving me confidence and exciting me about physics.

Additionally, I would like to thank Professor Mildred Dresselhaus, who appears to have an infinite amount of energy and patience, and she always been there for me through thick and thin. Dr. Gene Dresselhaus has also always made time to help me and to give me ideas and to answer all my questions, and I am thankful to him for that.

Finally, Georgii Samsonidze and Grace Chou have been incredibly kind to me and have helped me immensely to learn the theory and perform the experiments I needed for this work. They both have never been too busy to answer my questions and have often gone out of their way to make sure I had a thorough understanding of things.

Contents

List of Figures

List of Tables

Chapter 1

Introduction

Single wall carbon nanotubes (SWNTs) have come to occupy one of the central places in the rapidly developing science of low-dimensional systems and nanomaterials over the last decade due to their many unique physical, chemical and electronic properties. [1] They have shown remarkable signs of applicability for a number of future, technological applications, artificial muscles [2], scanning probes [3], and electron field emitters [4]. They are also unique as a prototype for modeling one-dimensional systems, the electronic and vibrational properties varying from tube to tube on the basis of their diameters and chiralities [1, 5].

In order to understand the physics of SWNTs, it is necessary to be able to ascertain - among other things - their diameter, chirality, metallicity and purity. Resonance Raman spectroscopy has proven to be a powerful, non-destructive tool that can measure all of these properties, and, in addition, due to the electronic structure of SWNTs, Raman spectroscopy is able to make measurements on individual SWNTs on a substrate. The rich Raman spectra of SWNTs contains several first-order and second-order features, each of with is able to tell us something about either the diameter, metallicity, or chirality of the SWNT being probed, or some combination of these.

In this thesis, the results of two resonant Raman experiments performed on SWNTs are presented and analyzed. In Chapter 2, the electronic and vibrational structure of graphite and SWNTs are explained and it is described how changing the

(n,m) geometry of an SWNT can also change its electronic properties. Additionally, the basic principles behind first-order and second-order Raman spectroscopy are presented and it is shown how to specifically apply them to graphite and SWNTs. In Chapter 3 we discuss two specific features of the Raman spectra for carbon materials, the M-Band and the iTOLA mode. By performing resonance Raman experiments on SWNT bundles and isolated SWNTs, the possible origins of these features are determined by using double resonance Raman theory. In Chapter 4, a theory is presented for determining the Fermi energy dependence of the frequency for certain Raman modes of SWNT materials. This theory is then applied to an electrochemical experiment where the Fermi energy was raised by application of an external voltage while Raman spectra were being taken *in situ*, and from these experimental data, certain constants for the theory are determined.

Chapter 2

Background

In this chapter we provide a rough explanation of the electronic and vibrational structures of a SWNT, explaining how they relate to two-dimensional graphite and the origin of the van Hove singularities in the joint density of electronic states. We also discuss the general theory of resonance Raman spectroscopy, and show specifically how it is applied to graphite and SWNTs.

2.1 Vibrational and Electronic Structure of SWNTs

The electronic joint density of states (JDOS) for a SWNT is dominated by the presence of van Hove singularities (VHS)(see Fig. B-5) at energies that are dependent on the diameter and chirality of the SWNT. To understand where these singularities lie, it is necessary to understand that a SWNT can be approximated as a hexagonal graphite sheet rolled into a small cylinder with a diameter of d_t ~1.0nm. Hence, we can obtain a good estimation of the 1-D electronic structure of a SWNT by starting with the 2-D electronic structure of graphite (shown in Fig. B-1) and then restricting electronic states to exist along certain one dimensional lines, called cutting lines. To understand why this is so, consider that an electron moving circumferentially around a small cylinder will interfere with itself except at certain wavelengths, hence, for smaller diameter SWNTs the distance between cutting lines will be greater. [5, 6]

For graphite, the smallest splitting between the valence and conduction bands

occurs at the **K**-point, where there is zero splitting, and where the energy contours are roughly circular, as shown in Fig. B-1. So, to calculate the JDOS for a SWNT near the Fermi energy, it is necessary to observe the cutting lines near the **K**-point of graphite. As shown in Fig. B-3, a VHS will occur wherever a cutting line tangentially touches one of these circular energy contours. We note as a matter of completeness, that a SWNT will be metallic whenever a cutting line cuts *through* the **K**-point. [5, 6]

This is not the entire story, however. In Fig. B-1, it is apparent that the energy contours around the **K**-point are not exactly circular, they become triangular at further and further distances. Because of this effect, cutting lines that are equidistant from the **K**-point will tangentially touch different energy contours, and thus the VHS of SWNTs with the same diameter can occur at different energies. This is illustrated in Fig. B-5 where the singularities in the JDOS of several metallic SWNTs with similar diameters but different (n,m) values are shown to differ. In Fig. B-17 is the so-called "Kataura" plot which plots the energy spacing between the first few VHSs as a function of diameter for all possible (n,m) values. [7]

The vibrational structure of a SWNT is determined in a very similar manner as the electronic structure, by first calculating the phonon energy contours for graphite, and then cutting the surface with 1-D cutting lines. Figure B-2 shows the phonon dispersion relations for graphite from the Γ to **K**-points. [5, 8]

2.2 Resonance Raman Spectroscopy

2.2.1 First-Order Resonance Raman Spectroscopy

An electron that has been excited from the valence to the conduction band will often interact with the phonons of the material before recombining with the hole in the valence band, and re-emitting a photon in the process of returning to equilibrium. If an electron with wave vector k interacts with some phonon with wave vector q, then by either phonon emission or phonon absorption, the electron will be scattered to some new state $k - q$ or $k + q$, respectively, and the energy of the re-emitted photon

will be shifted downward or upward by $\hbar\omega_q$. If only one phonon scattering event occurs, this is called a first-order Raman process, and if either the state k or $k \pm q$ is a real state, then the process is called a first-order resonance Raman process (shown in Fig. B-6(a1-a2)). One important restriction for a first-order process is that the excited electron must return to its original k in order to recombine with the hole at the k state. Hence, only $q \sim 0$ phonon wave vectors are selected in a first-order Raman process, and these wave vectors correspond to points near the Γ-point in Fig. B-2. [9]

For SWNTs, Raman spectra taken from metallic and semiconducting SWNTs with E_{L}=1.58 eV are shown in Fig. B-4. In these spectra, the radial breathing mode (RBM) and the G-band represent first-order Raman processes. The higher frequency G-band is produced by longitudinal and tangential phonons, ("LO" and "iTO" in Fig. B-2) and it is observed in many graphitic materials as a single spectral feature. For SWNTs, however, the G-band appears as a multiple peak structure. Its lower frequency G^- component exhibits a Breit-Wigner-Fano (BWF) lineshape for metallic (M) SWNTs and a Lorentzian lineshape for semiconducting (S) SWNTs. [10] The origin of the BWF G^- feature is attributed to the coupling of collective electronic excitations, called plasmons, in both isolated and bundled M SWNTs to the transverse in-plane phonon modes.[11] Because of the collective electronic effects and the role of intertube interactions in giving rise to the BWF lineshape for the G^- feature in M SWNTs, the intensity of the G^- feature depends non-linearly on the number of M SWNTs in the sample and within a SWNT bundle. The G^- feature thus provides "coupled" information both on the relative number of M SWNTs in the sample and on the average number of M SWNTs within the bundles.

The RBM, however, is a feature unique to SWNTs and is produced by the radial contracting and expanding of the SWNT. The frequency of the RBM is related to the diameter of the SWNT by the relation:

$$\omega_{RBM} = \frac{\alpha}{d_t} + \beta\,, \tag{2.1}$$

where α and β are dependent on the SWNT environment (i.e. substrate and bundling effects). For isolated SWNTs grown by CVD on Si/SiO_2 substrates, it has been

determined that α=248cm^{-1} and β=0 [12], while α=239 cm^{-1}nm and β=8.5 cm^{-1} have been reported for HiPco SWNTs in bundles. [13] Once this relation has been determined, the (n,m) value for an isolated SWNT whose Raman spectra was taken at E_{L} can be closely estimated from it's RBM frequency, ω_{RBM}, using Eq. 2.1 and the Kataura plot shown in Fig. B-17.[12]

2.2.2 Double Resonance Raman

In an arbitrary second-order Raman process, an electron in the k state will first get scattered by -q, and then will be scattered by +q (or vice versa) to return back to its original k state. This allows for the possibility of $q \neq 0$, so that phonons away from the Γ-point can now contribute to the Raman signal. The probability, however, for an electron to get scattered by a specific q value is low. Hence, for arbitrary q, it is very unlikely that a single electron will get scattered by both +q and -q. [9]

In a double resonance Raman scattering process, however, the electron is still scattered twice, but the Raman intensities are almost the same as for a first-order resonance process. [14] A double resonance scattering can be the result of a second-order Raman process where either the initial k state and the $k+q$ state are both real electronic states; or, the final k state and the $k+q$ state are both real electronic states (see Fig. B-6(c1-c2)). Additionally, a double resonance scattering process can be a one phonon process where the second scattering is a defect scattering event, which causes no change in energy. In this case, there are four resonant conditions where the intermediate state $k+q$ is real and either the initial k state or final k state is real; and the defect scattering and real phonon scattering can occur in either order, as shown in Fig. B-6(b1-b4). [9]

Since a double resonance process is no longer a single scattering process, there are many more real electronic states available for an electron in the intermediate state, $k+q$, to scatter to. Specifically, the intermediate state can now exist anywhere on the energy contour where the energy is close to E^i(k), the energy of the initial k state. For 2-D graphite, this means that the intermediate state $k+q$ can exist either around the original **K**-point (near the initial k state) or $k+q$ can exist around the inequivalent **K'**-

point (see Fig. B-1); we call these two processes intravalley and intervalley scattering processes, respectively. The phonons, with wavevector q, involved with intravalley scattering originate from the Γ-point, while those involved with intervalley scattering originate from the **K**-point. [8] Note also, that restricting the intermediate state $k+q$ to have energy $\sim$E^i(k) causes q to be dependent on k through some relation. In the case of graphite, due to the linear electron energy bands near the **K**-point, this relation has been shown to be $q \sim 0$ or $q \sim 2k$ from either the **K** or Γ-points. [15, 8, 16, 17] The result of these relations, means that by observing how the positions of double resonant Raman modes change with different laser energies, it is possible to use $q \sim 2k$ to probe the phonon dispersion relations for graphite from the **K**-point and the Γ-point, as is shown in Fig. B-2. [8]

Of the SWNT Raman features shown in Fig. B-4, the D-band, G'-band, iTOLA mode, and the M-Band are all double resonance Raman features, and all occur in both graphite and SWNTs. The iTOLA mode and M-band will be discussed in Ch. 3. The D-band, which occurs at $\sim$1355cm^{-1} for E_{laser}=2.41 eV, is produced from the LA phonon mode near the **K**-point (see Fig. B-2) and has been shown to be defect related through experiments where defects were introduced to graphitic and SWNT samples and where the D-band intensity increased and eventually became comparable to that of the G-band [18, 19, 20, 21, 22]. The G'-band, which occurs at $\sim$2700cm^{-1} for E_{laser}=2.41 eV, is the first overtone of the D-band and therefore does not require the presence of a defect.[15, 16, 23, 24, 25] Thus, the D-band is a one-phonon second-order process, while the G'-band is a two-phonon second-order process. By varying the laser excitation energy, E_{laser} , within the visible light energy range, the Raman frequency dispersion relations have been shown to be $\partial\omega_{\rm D}/\partial E_{\rm laser} = 53{\rm cm}^{-1}/{\rm eV}$ and $\partial\omega_{\rm G'}/\partial E_{\rm laser} = 106{\rm cm}^{-1}/{\rm eV}$.[20, 21, 26, 27]

Chapter 3

Second-order harmonic and combination modes in graphite, SWNTs in bundles and isolated SWNTs

3.1 Introduction

In this chapter we study weak Raman features observed in the frequency range 1650–2100 cm^{-1} in graphite-related materials (i.e., HOPG, SWNT bundles and isolated SWNTs), and we show that these features are related to overtones and combination modes of the several phonon branches in graphite, as predicted by double resonance theory [8].

In particular, we consider here a multi-featured band at about 1750 cm^{-1}. This band was previously observed, but until now unassigned, in HOPG [28], in irradiated graphite [29], and it is also observed in SWNT bundles, where it was tentatively assigned as a combination mode of the G band and the radial breathing mode (RBM) [30]. We assign this feature in the present work to an overtone of the infrared-active out-of-plane (oTO) mode at 867 cm^{-1} in graphite. The oTO mode has been

observed in Raman spectra taken along the broken edges of HOPG [31] and in SWNTs [32]. In addition, we report a very highly dispersive mode at higher frequencies (around 1950 cm^{-1}) that has previously been reported for SWNT bundles [30], and we tentatively identify this mode as a combination of the in-plane transverse optic (iTO) and longitudinal acoustic (LA) modes, namely (iTO+LA). The results for both the features around 1750 cm^{-1} and the feature around 1950 cm^{-1} provide experimental evidence for the predictions of double resonance Raman theory for overtones and combinations of modes [8]. In the case of isolated SWNTs, the multi-featured band at 1750 cm^{-1} shows a richer behavior than in HOPG (and is more complicated than the D-band and the G'-band in isolated SWNTs [33, 34]), varying from tube to tube, thus suggesting a strong dependence on the one-dimensional structure of SWNTs.

3.2 Experimental Details

Raman spectra for HOPG and isolated SWNTs were acquired under ambient conditions, using a single monochromator Renishaw 1000B spectrometer equipped with a cooled Charge Coupled Device (CCD) detector and notch filters, in a back scattering configuration. The excitation laser line $E_{laser} = 2.41$ eV from an Ar laser was used for HOPG and for the isolated SWNTs. Data from SWNT bundles ($d_t = 1.49 \pm 0.20$ nm as determined from transmission electron microscope measurements) obtained with the laser excitation energy $E_{laser} = 1.58$, 1.96, 2.41 and 2.71 eV by Brown et al. [30] were used in our analysis to study the dependence of the various features on E_{laser}.

Isolated SWNTs were prepared by a chemical vapor deposition (CVD) method on a Si/SiO_2 substrate containing nanometer size iron catalyst particles [12, 35]. Atomic force microscopy (AFM) was used to characterize the isolated SWNT sample, showing that the SWNTs ranged in diameter from 1 to 3 nm, and had lengths ranging from a few hundred nm up to 2μm. The AFM images showed a very low SWNT density (~40 nanotubes/100μm^2), and showed that most of the SWNTs did not touch one another. We measured the Raman spectra from more than 100 isolated SWNTs resonant with $E_{laser} = 514.5$ nm (2.41 eV). Of all the spectra taken, the

spectra from only 51 tubes were used to conduct this study, since the $\sim 1750\,\mathrm{cm}^{-1}$ Raman feature was not observed in many of the spectra. Of these 51, not all tubes were used in each part of the study, since the spectra from some tubes did not show an observable radial breathing mode (RBM) feature, which we used for the nanotube diameter determination (using the relation $d_t = 248/\omega_{\mathrm{RBM}}$) and for the tentative (n, m) assignments based on Ref. [12].

3.3 Results and Discussion

3.3.1 General Results

The top three traces in Fig. B-7 show Raman spectra between $1650\,\mathrm{cm}^{-1}$ and $2100\,\mathrm{cm}^{-1}$ from HOPG, SWNT bundles, and an isolated SWNT, using $E_{\mathrm{laser}} = 2.41\,\mathrm{eV}$. This laser line excites semiconducting SWNTs predominantly, considering the SWNT diameters and diameter distributions contained in the various samples. All the spectra in Fig. B-7 show the presence of a multi-featured band at about $1750\,\mathrm{cm}^{-1}$ whose origin had not yet been assigned in the literature prior to our work. (We here call this band the M band reflecting the two-peak visual shape of this band). This M band in HOPG and for the isolated (15,7) SWNT (second trace from the bottom in Fig. B-7, and with a diameter $d_t = 1.52\,\mathrm{nm}$) clearly shows two components. The lowest trace in Fig. B-7 shows the average of this M feature in the summation of Raman spectra taken from 51 isolated SWNTs (mean diameter $= 1.6\,\mathrm{nm}$), and we can fit the resulting asymmetric lineshape with two Lorentzian peaks. The asymmetric lineshape in Fig. B-7 for SWNT bundles is likewise fit to two Lorentzian peaks. All four examples of this M band in Fig. B-7 exhibit a similar splitting of $\sim 20\,\mathrm{cm}^{-1}$ at $E_{\mathrm{laser}} = 2.41\,\mathrm{eV}$, but the average M-band frequencies are somewhat upshifted (or downshifted) from each other, probably due to the presence or absence of bundle interactions and curvature effects. However, the agreement between the frequencies of the two M-band features from the SWNT bundle and the isolated $(15, 7)$ SWNT suggests a weak contribution from the intertube interaction. A summary of this anal-

ysis is in Table A.1 for the upper (ω_M^+) and lower (ω_M^-) frequency components and for the splitting $\Delta\omega_M = \omega_M^+ - \omega_M^-$. For all nanotubes in Table A.1, d_t is determined from the radial breathing mode frequency, using the relation $\omega_{\rm RBM} = 248/d_t$ [12], and averaged values are given for SWNT bundles and for the summation spectrum from the 51 isolated SWNTs.

Previously, this M feature was tentatively assigned to a combination mode of the G band and RBM features ($\omega_G + \omega_{\rm RBM}$) [30]. However, as can be seen in Fig. B-7, the presence of this feature in HOPG, which has no RBM, indicates that a different explanation for this feature is needed.

Another very weak feature can also be seen in the spectrum in Fig. B-7 for HOPG and SWNT bundles above 1950 $\rm cm^{-1}$. We will call this (iTO + LA) feature iTOLA, as explained below. Previously, this feature was tentatively assigned as a combination mode ($\omega_G + 2\omega_{\rm RBM}$). [30] Once again, a different explanation is needed, since this feature is observed also in HOPG. Furthermore, as shown in Ref. [30], this feature is strongly dispersive, in disagreement with the ($\omega_G + 2\omega_{\rm RBM}$) tentative assignment in Ref. [30], as we discuss below.

3.3.2 Mode Assignments

To help with the identification of the origin of the features near 1750 $\rm cm^{-1}$ (M) and near 1950 $\rm cm^{-1}$ (iTOLA) in Fig. B-7, an analysis of the dependence of the spectra on $E_{\rm laser}$ was carried out to determine the dispersion of these spectral features as $E_{\rm laser}$ is varied. Such information can be deduced from the spectra in Ref. [30] on SWNT bundles. Figure B-8 shows that the M feature near 1750 $\rm cm^{-1}$ can be analyzed in terms of two components with frequencies ω_M^- and ω_M^+. A Lorentzian fit was therefore made of the several Raman features observed from 1650 to 2100 $\rm cm^{-1}$ from SWNT bundles, using different $E_{\rm laser}$ excitation lines. This figure shows that the lower frequency mode ω_M^- exhibits a weakly dispersive behavior (frequency ω_M^- shifting down by $\sim$ 30 $\rm cm^{-1}$ as $E_{\rm laser}$ is varied from 1.58 eV to 2.71 eV), while the upper feature frequency ω_M^+ is basically independent of $E_{\rm laser}$. [36] The higher frequency iTOLA mode is highly dispersive and upshifts from 1864 $\rm cm^{-1}$ to 2000 $\rm cm^{-1}$ as $E_{\rm laser}$ varies from

1.58 eV to 2.71 eV.

Well-known frequency dispersive modes in graphite-related materials are the disorder-induced D band, and its second-order feature, the G' band. Their appearance and dispersive behavior were recently explained as due to a double resonance process [15]. Saito et al. [8] subsequently applied the double resonance theory developed for the D/G' bands to all the phonon branches of graphite, and showed that many low intensity dispersive and non-dispersive features are expected to appear in the Raman spectra of graphite-related materials, reflecting the vibrational and electronic structure of the material. Although they only applied the double resonance theory to one-phonon processes explicitly, the corresponding mechanisms can be applied to two-phonon processes, giving rise to combination modes and overtones, like the G' band [8, 15]. As we discuss below, we propose here that the features observed between 1650 and 2100 cm^{-1} are overtones and combination modes related to graphite, as predicted by double resonance theory [8]. More specifically, the two features near 1750 cm^{-1} (M band) are attributed to overtones of the out-of-plane (oTO), infrared-active mode at 867 cm^{-1} in graphite [31], and the feature at $\sim$1950 cm^{-1} (iTOLA band) is attributed to a combination of one phonon from the in-plane transverse optical branch (iTO) plus one phonon from the longitudinal acoustic (LA) branch, iTO+LA.

Figure B-9(a) shows the phonon dispersion curves for graphite from the Γ-point to the K-point of the 2D graphite Brillouin zone from Ref. [8]. Also plotted in Fig. B-9(a) are the predicted dispersion relations for the second-order overtone of the out-of-plane optical (oTO) mode (related to the $M^{\pm}$ bands) and for the second-order combination mode corresponding to the (iTO + LA) or iTOLA band. The experimental points are plotted in Fig. B-9(a) as a function of phonon wave vector q according to double resonance theory [8], as discussed in the next paragraphs. Note that the agreement between the experimental and theoretical frequencies for the overtone (M) and combination (iTOLA) bands is very good.

Assuming that the M band is an overtone of the band near $\omega_{\mathrm{oTO}} = 867\,\mathrm{cm}^{-1}$ in graphite, if we change the laser excitation energy (E_{laser}), we should be able to reproduce the phonon dispersion relations of graphite, as described by Saito et al.

[8]. The two allowed double resonance processes in Ref. [8] correspond to $|q| \simeq 0$ and $|q| \simeq 2|k|$, where k and q denote, respectively, the electron wave vector measured from the K point, and the phonon wave vector measured from either the Γ (intra-valley process) or the K point (inter-valley process). The wave vectors $|q| \simeq 0$ do not depend on E_{laser}, while the wave vectors $|q| \simeq 2|k|$ vary significantly with E_{laser} in order to satisfy the double resonance condition.[8] From the known dispersion relations for graphite $\omega(q)$ [see Fig. B-9(a)], we see that the phonon branch oTO, which is responsible for this mode, decreases in frequency as q moves away from the Γ-point. We should therefore expect that the M band would have two components: a lower frequency component, ω_M^-, which is associated with the $|q| \simeq 2|k|$ double resonance process and which decreases in frequency with increasing E_{laser}, and a higher frequency component, ω_M^+, which is associated with the $|q| \simeq 0$ double resonance process, and ω_M^+ is independent of E_{laser}, in agreement with the experimental observations for ω_M^+ and ω_M^- in Fig. B-8.

In Fig. B-9(b) we plot the experimental results of Fig. B-8 for the feature observed near $1750\,\text{cm}^{-1}$ in SWNT bundles as a function of E_{laser} (lower scale), using ($\square$) for ω_M^+ and ($\triangle$) for ω_M^-. Using the upper scale in Fig. B-9(b), we plot the $|q| \simeq 2|k|$ values for the M^- and iTOLA bands (the upper scale does not apply to ω_M^+, where $q \simeq 0$), corresponding to a given E_{laser} (see Ref. [8]). The connection between the two scales in Fig. B-9(b) (lower E_{laser} and upper q) follows from the linear relation between E_{laser} and q, namely $E_{\text{laser}} = (\sqrt{3}/2)\gamma_0 aq$, which in turn comes from the electron dispersion relation around the K-point and the double resonance condition $|q| \simeq 2|k|$. For comparison, we plot the frequencies (solid lines) according to predictions from double resonance theory for the two $\omega_M^{\pm}$ branches. The theoretical curves for ω_M^- and ω_M^+ in Fig. B-9(b) are upshifted by $20\,\text{cm}^{-1}$, as discussed below, to match the experimental observations of $\omega_M^{\pm}$ for SWNT bundles. Note that, except for the $20\,\text{cm}^{-1}$ constant upshift of the theoretical $M^{\pm}$ dispersion curves, the agreement between theoretical predictions for ω_M^- and ω_M^+ and the experimental observations is very good. Both experimental and theoretical values exhibit the same dispersion for the M^- feature, and the same magnitude of the $\Delta\omega_M \sim 20\,\text{cm}^{-1}$ splitting (for $E_{\text{laser}} = 2.41\,\text{eV}$) that

is observed for all samples in Fig. B-7 (see Table A.1). Also plotted in Fig. B-9(b) are the points observed for $\omega_M^{\pm}$ for HOPG at $E_{\text{laser}} = 2.41\,\text{eV}$ (denoted by a filled square and a filled triangle) which are seen to be upshifted by $20\,\text{cm}^{-1}$ from the $\omega_M^{\pm}$ observed for the SWNT bundles. However, the splitting $\Delta\omega_M$ between ω_M^- and ω_M^+ is the same for SWNT bundles, HOPG, and in the theory.

The calculated ω_M^+ and ω_M^- as a function of E_{laser} in Fig. B-9(b) show that $\Delta\omega_M = \omega_M^+ - \omega_M^- \simeq 20\,\text{cm}^{-1}$ for $E_{\text{laser}} = 2.41\,\text{eV}$, in good agreement with experiment, but Fig. B-9(b) also predicts that $\Delta\omega_M$ should increase with increasing E_{laser}. Raman spectra for irradiated graphite [29] using $E_{\text{laser}} = 5.0\,\text{eV}$ (248 nm) show two features in the frequency range of the M band, with an estimated splitting of $\Delta\omega_M \sim 70\,\text{cm}^{-1}$. Using published force constant models [8, 37], $\Delta\omega_M$ at $E_{\text{laser}} = 5.0\,\text{eV}$ ($q = 0.53K$) can be estimated, yielding $\Delta\omega_M \sim 148\,\text{cm}^{-1}$ for the force constants used in Ref. [8] which does not include double resonance Raman data, and $\Delta\omega_M \sim 96\,\text{cm}^{-1}$ for the force constants used in Ref. [37] based on double resonance Raman data, but does not include data for the Raman M bands in the force constant fitting procedure. At present the force constant models are not sufficiently accurate to predict $\Delta\omega_M$ for such large q values (or E_{laser} values as large as 5.0 eV). The two force constant models (Refs. [8, 37]), which are based on fitting two rather different sets of experimental data, show large differences in their predictions of $\Delta\omega_M$ at 5.0 eV. Further improvements in the force constant models (perhaps including $\Delta\omega_M$ data for fitting inputs) are needed to fit the $\Delta\omega_M$ dispersion at large E_{laser} values.

In Fig. B-9(b) we also plot the frequencies for the combination of the in-plane transverse optical mode (iTO) and the longitudinal acoustic mode (LA), as predicted by double resonance theory (dark solid line) for $|q| \simeq 2|k|$. To compare these predicted values for the iTO+LA frequencies, we plot in Fig. B-9(b) the highly dispersive iTOLA mode frequencies ($\diamondsuit$) observed in Fig. B-8 between 1864 and $2000\,\text{cm}^{-1}$. We see that the agreement between this observed highly dispersive iTOLA mode frequency and the theoretical predictions for iTO+LA is very good (thus explaining the choice of the name iTOLA for this mode). Note that for this combination mode we do not expect to observe the double resonance feature related to $|q| \simeq 0$, since $\omega_{\text{LA}} = 0$ and

$\omega_{\text{iTO}} = \omega_{E_{2g}} = 1582\,\text{cm}^{-1}$ for $|q| \simeq 0$.

Although the M features observed in SWNT bundles and in HOPG for $E_{\text{laser}} = 2.41\,\text{eV}$ are similar, there is an upshift of about $20\,\text{cm}^{-1}$ in the experimentally observed ω_M for HOPG compared with SWNT bundles. We attribute this difference in the observed ω_M between HOPG and SWNTs to a diameter dependent curvature effect in the cylindrical SWNTs. A related effect is observed in the G-band leading to a downshift in ω_G^-, corresponding to circumferential vibrational displacements, relative to ω_G^+ which corresponds to displacements along the SWNT axis [38, 39]. A related effect is also observed in measurements on the D and G'-band frequencies in SWNTs, for which a downshift in these mode frequencies is found to be proportional to $1/d_t$ [40, 41, 42], and this effect is discussed further below, in Sect. 3.3.3, in connection with the $M^{\pm}$ bands.

Also plotted in Fig. B-9(b) are all the other possible overtones and combination modes for two phonons associated with the Γ-point (long dashed lines) and with the K-point (dashed lines) according to double resonance theory [8]. One can see that the solid curves (M^+, M^- and iTOLA) represent the best mode assignments for the experimental features. While the double resonance theory accounts well for the behavior of the mode frequencies for $E_{\text{laser}} < 3.0\,\text{eV}$, it is interesting to note that the intensity of the double resonance Raman bands remains an open issue.

Figure B-9(a) thus gives us a more complete picture than was previously available for the phonon dispersion in graphite-like materials which can be used to interpret experimental second-order Raman spectra taken with different laser excitation energies, thereby giving more detailed information than in Ref. [8] about the various double resonance Raman processes associated with the Γ point. In particular, Fig. B-9(a) includes two additional dispersion curves, one for the M feature (identified as a harmonic of the out-of-plane infrared active mode in graphite) and a second for the iTOLA feature which is a combination (iTO + LA) mode. Whereas previous studies were predominantly focused on double resonance effects associated with phonons near the K-point in the Brillouin zone (the D-band and the G'-band), the present work focuses on double resonance processes for non-zone center phonons connected with

the Γ-point.

3.3.3 Isolated SWNTs

Figure B-10 shows spectra in the 1300–2000 cm^{-1} range taken from several isolated SWNTs. These spectra all show the M band as well as the G band, and in some cases weak D-bands are also seen. For each spectrum in Fig. B-10 the RBM feature was observed and the RBM frequency is given on the figure, so that (n, m) indices could be tentatively assigned to each tube, based on the RBM frequency [12] and on other diameter and chirality-dependent Raman features [33, 34, 39, 43]. From Fig. B-10 we see that even though the same E_{laser} is used for all spectra ($E_{\mathrm{laser}} = 2.41\,\mathrm{eV}$), the details of the spectra of the M band at the single nanotube level vary significantly from one (n, m) nanotube to another.

Many of the nanotubes show two clear features ($\omega_M^{\pm}$), but some tubes show only one well-defined feature. In Fig. B-10 we observe two tubes both with $\omega_{\mathrm{RBM}} = 180\,\mathrm{cm}^{-1}$, one showing a strong M band at $1741\,\mathrm{cm}^{-1}$, while the second one has a broader M band at $1753\,\mathrm{cm}^{-1}$ with a very different lineshape. At $\omega_{\mathrm{RBM}} \approx 130\,\mathrm{cm}^{-1}$, we see two tubes again with similar ω_{RBM} values, and while the first has two well-defined peaks at $1738\,\mathrm{cm}^{-1}$ and $1768\,\mathrm{cm}^{-1}$, the second tube contains only one well-defined peak at $1752\,\mathrm{cm}^{-1}$, with a different lineshape. In these cases, tubes with similar ω_{RBM} values, but with different M band features, were identified as tubes having different (n, m) values. These assignments are supported by the analysis of other diameter and chirality-dependent Raman features for these nanotubes [33, 34, 39, 43].

There are, however, other cases where tubes with approximately the same d_t also show similar M bands, as, for example, the two nanotubes with $\omega_{\mathrm{RBM}} \approx 160\,\mathrm{cm}^{-1}$ where both nanotubes contain a double-featured M band at $1731\,\mathrm{cm}^{-1}$ and $\approx 1751\,\mathrm{cm}^{-1}$. The tubes with $\omega_{\mathrm{RBM}} \approx 160\,\mathrm{cm}^{-1}$ were here tentatively assigned to the same *(n,m)* values. The assignments in this case are also supported by the similarity of other diameter and chirality-dependent Raman features for these two nanotubes [33, 34, 39, 43]. The small differences we observe comparing the two traces tentatively assigned as $(15, 7)$ SWNT in Fig. B-10 are probably due to nanotube defects, as suggested by the

different intensities for the D bands shown by those spectra, and may also be due to differences in the polarization of the light with respect to the tube axis (see Ref. [44]).

It is interesting to note also that, at the single nanotube level, the $\Delta\omega_M \approx 20\,\mathrm{cm}^{-1}$ separation between the M^+ and M^- features using $E_{\mathrm{laser}} = 2.41\,\mathrm{eV}$ does not hold exactly, as can be seen in Fig. B-10. For example, $\Delta\omega_M = 36\,\mathrm{cm}^{-1}$ for the SWNT tentatively assigned as $(10, 9)$, $\Delta\omega_M = 20\,\mathrm{cm}^{-1}$ for the $(15, 7)$ tube, and $\Delta\omega_M = 30\,\mathrm{cm}^{-1}$ for the (22,3) tube. However, the average value of $\Delta\omega_M$ over the 51 SWNTs is $\Delta\omega_M = 22\,\mathrm{cm}^{-1}$, in good agreement with the results of Fig. B-8 showing $\Delta\omega_M = 23\,\mathrm{cm}^{-1}$ for SWNT bundles. This comparison further shows the connection between results for individual isolated SWNTs, the average of isolated SWNTs, and the corresponding results for SWNT bundles.

The dispersive feature observed in the 1950–2000 cm^{-1} range in SWNT bundles, as shown in Fig. B-8, was rarely seen in isolated tubes due to the low intensity of this feature. For example, the spectrum assigned as $(23, 1)$ in Fig. B-10 shows this feature at $1983\,\mathrm{cm}^{-1}$, consistent with the data for the SWNT bundles [30]. We do not have an explanation for our infrequent observation of the iTOLA feature in isolated SWNTs.

Figure B-11 plots ω_M (open squares and open triangles) against $(1/d_t)$, as obtained from the radial breathing mode feature $d_t = 248/\omega_{\mathrm{RBM}}$ [12], for 36 of the isolated SWNTs for which the Raman spectra contained both the M band *and* the RBM features. The open square symbols are used for the higher frequency M^+ peak in the M band when two peaks are observed. The filled square and filled triangle corresponding to $(1/d_t) = 0\,\mathrm{nm}^{-1}$ represent the ω_M^+ and ω_M^- frequencies observed in HOPG. No clear diameter dependence can be deduced from the data in Fig. B-11, indicating that the frequencies $\omega_M^{\pm}$ for isolated SWNTs are very sensitive to chirality, thus supporting a double resonance mechanism for the M band.

The stars (*) in Fig. B-11 indicate the frequency expected at $q \simeq 0$ from the combination mode $\omega_G^+ + \omega_{\mathrm{RBM}}$ for each SWNT spectrum, while the crosses ($\times$) indicate the lower frequency combination mode $\omega_G^- + \omega_{\mathrm{RBM}}$. Here ω_G^+ and ω_G^- are the frequencies of the G band peaks ($q \simeq 0$) at about $1591\,\mathrm{cm}^{-1}$ and $1570\,\mathrm{cm}^{-1}$, respectively,

corresponding to displacements along the tube axis (ω_G^+) and in the circumferential direction (ω_G^-).[38, 39] Figure B-11 shows that the M and the RBM+G mode frequencies for some SWNTs fall in the same frequency range, but not close enough in general to explain the data points themselves. Considering the $|q| \simeq 2|k|$ double resonance condition, the RBM+G modes should also vary in frequency from tube to tube, as observed for the M bands in Fig. B-11, due to the different zone folding for different (n, m) nanotubes.[5] However, the RBM+G combination modes away from $q = 0$ are predicted to appear at considerably higher frequencies due to the positive dispersion of the acoustic branches.

There is one point in Fig. B-11 that is far away from the others (at $1/d_t \sim 1.1\,\mathrm{nm}^{-1}$). This point corresponds to the uppermost spectrum in Fig. B-10 and is identified with the (11,2) SWNT. This SWNT is metallic and shows a strong M band spectral feature. The apparent difference in ω_M for this SWNT relative to all the others might be due to the fact that this SWNT exhibits a very small diameter ($d_t < 1\,\mathrm{nm}$), where phonons and plasmons interact strongly, thus generating an overdamped behavior, as shown by the large intensity Breit–Wigner–Fano component observed in the G^- band (see Fig. B-10 and Refs. [45] and [39]). Further experimental study of such metallic tubes is needed.

From Figs. B-10 and B-11, we conclude that different (n, m) SWNTs show very different M bands, similar to the case of the D and G' bands in isolated SWNTs [33, 34]. These results suggest that the $M^{\pm}$ features also have a strong (n, m) dependence (including a dependence on both tube diameter and chirality), as in the case of the D and G' bands. This (n, m) dependence comes from the fact that in 1D SWNTs the double resonance conditions $q \simeq 0$ and $|q| \simeq 2|k|$ are limited by the possible q (and k) wave vectors that are available for this 1D system [5], and the observation of the resonance Raman effect from isolated SWNTs is further limited by the $E_{\mathrm{laser}} \sim E_{ii}$ resonance condition [12]. Unlike the situation in 2D graphite, it is not generally possible to satisfy both the resonance Raman condition and the restricted q vectors simultaneously in isolated SWNTs.

Furthermore, the physics involved in the M band case seems to be more compli-

cated than for the D and G' bands. In the case of the D and G' bands, it is clear which modes are involved in the process, probably because the scattering processes mediated by the D band phonons exhibit a very strong matrix element. In the case of the low intensity M and iTOLA features, many overtone and combination modes [such as the (G + RBM) combination mode] can appear in the same frequency range, as shown in Fig. B-9(b) by the dotted/dashed curves (or in Fig. B-11 by the * and $\times$ points), and they can be resonantly enhanced differently for different (n, m) SWNTs.

To gain insight into whether two features or one feature occur in the spectral band near $1750\,\mathrm{cm}^{-1}$, we plot in Fig. B-12(a) the experimental frequencies ω_M against the energy of the van Hove singularity E_{ii} as calculated from (n, m) values assigned to each tube. We use the $\square$ symbol for ω_M^+ when two features are clearly observed in the spectra, and we use the $\triangle$ symbol for ω_M^-. From 36 SWNTs that exhibit both M and RBM features, we plot here data only for the 21 SWNTs for which we can make confident (n, m) assignments; for the other 15 tubes, the quality of the other Raman features (RBM, G and G′ bands) are sufficient to determine d_t, but not good enough to obtain an unambiguous (n, m) assignment. We see that for tubes having $E_{ii} < 2.41\,\mathrm{eV}$, both $\omega_M^{\pm}$ modes are usually observed. For tubes with $E_{ii} \geq 2.41\,\mathrm{eV}$, only one feature (ω_M^-) is usually observed experimentally. Two M features are observed for only two SWNTs with $E_{ii} > 2.41\,\mathrm{eV}$, and, in both cases, the observed ω_M^+ frequencies satisfy the combination $\omega_G^+ + \omega_{RBM}$ expected according to the ω_{RBM} and ω_G frequencies observed for these SWNTs [see * in Fig.B-12(a)]. Therefore, the experimental results suggest that only one peak (M^-) is observed for $E_{ii} \geq E_{\mathrm{laser}}$, while both M^+ and M^- are observed for $E_{ii} < E_{\mathrm{laser}}$.

Figure B-12(b) presents a simple model to explain the phenomena reported in Fig. B-12(a), namely the existence of a threshold $E_{ii} = E_{\mathrm{laser}}$ for the appearance of the M^+ peak, that in 2D graphite corresponds to the $q \simeq 0$ double resonance condition. Neglecting the trigonal warping effect [7] on a 2D graphene sheet, the equi-energy contour for electronic/hole states in the conduction/valence band, resonantly excited by E_{laser}, corresponds to a circle in k space, centered at the K point. In the case of SWNTs, the available 2D-k space is limited in 1D to E_i cutting lines due to

the circular boundary condition along the circumference of the SWNT.[5] In Fig. B-12(b) we draw such an equi-energy circle about the K point and two 1D E_i cutting lines. The right box shows a 2D figure (k_x, k_y) and the left box shows a 3D figure (Energy, k_x, k_y). The cutting lines cross the circle, meaning that, for the specific (n, m) SWNT represented in the figure, E_{ii} ($\times$ indicates the corresponding k_{ii} at the van Hove singularity) is smaller than E_{laser}. The crossing points of the 1D cutting lines with the circle represent the SWNT electronic states that can be resonantly excited by E_{laser}. To have a *double* resonance process, a phonon must bring the excited electronic state to another real electronic state. For the SWNT, only a few phonons can satisfy the double resonance requirement and these phonons are explicitly indicated in the figure. Starting from a resonantly excited electronic state indicated by "1", phonon $q_{1\to 2}$ brings the electron resonantly to the real state "2". In the case of a Stokes scattering process, state "2" actually corresponds to a circle of smaller radius due to the smaller energy of the scattered electron. As a first approximation, we can ignore the small change in the radius of the constant energy contour in going from state "1" to state "2", and we consider both states to be on the same circle in Fig. B-12(b). This $q_{1\to 2}$ phonon satisfies the double resonance requirement for $q \simeq 0$. The two phonons $q_{1\to 3}$ and $q_{1\to 4}$ bring the electron resonantly to the real states "3" and "4", which both correspond to the double resonance requirement $|q| \simeq 2|k|$.

Considering $E_{\text{laser}} = 2.41\,\text{eV}$ and $\partial\omega_M/\partial E_{\text{laser}} \sim -25\,\text{cm}^{-1}/\text{eV}$, the difference between $q_{1\to 3}$ and $q_{1\to 4}$ is about $1\,\text{cm}^{-1}$, which is too small to be resolved experimentally, so that we would expect to observe only one feature in the Raman spectra, which we have called M^-. However, $q_{1\to 2}$ for $E_{\text{laser}} = 2.41\,\text{eV}$ is about $20\,\text{cm}^{-1}$ higher than $q_{1\to 3,4}$, thus allowing the M^+ peak to be distinguished from the M^- peak experimentally. It is clear that as E_{ii} approaches E_{laser}, the state "1" approaches "2", and the state "3" approaches "4" so that the $q \simeq 0$ double resonance effect disappears when "1" = "2", thus explaining the threshold at $E_{ii} = E_{\text{laser}}$ for the observation of the M^+ feature.

The solid curves in Fig. B-12(a) represent predicted frequencies for the processes $1 \to 2$, $1 \to 3$, and $1 \to 4$ discussed above. The phonon wavevectors $q_{1\to 2}$, $q_{1\to 3}$, and

$q_{1\to4}$ as a function of E_{ii} are determined from a simple geometrical construction shown in Fig. B-12(b). The predicted frequencies are obtained from the phonon dispersion curves for graphite [8] as two times the oTO mode frequency for a given phonon wavevector. The resulting predicted frequency is further upshifted by $40\,\mathrm{cm}^{-1}$ to satisfy the experimental points shown in Fig. B-12(a). Further refinements in the force constant model[5] are needed to account for this $40\,\mathrm{cm}^{-1}$ upshift in the theoretical curves.

Part of the experimentally observed upshift of the frequencies $\omega_M^{\pm}$ in graphite relative to SWNTs, comes from the dependence of these mode frequencies on nanotube diameter d_t. However, a simple plot of $\omega_M^{\pm}$ vs. $1/d_t$ for each individual SWNT would not yield a clear picture of the d_t dependence of these mode frequencies, because $\omega_M^{\pm}$ at the single nanotube level not only depends on nanotube diameter d_t, but also depends on other variables, such as nanotube chirality [expressed by (n,m)], E_{ii} and $E_{ii} - E_{\mathrm{laser}}$. We have, however, found in analyzing similar effects at the single nanotube level for the D-band and G'-band features [41, 42] that when the mode frequencies are averaged over chirality, by averaging ω_D and $\omega_{G'}$ over a significant number (> 10) of SWNTs which are each resonant with a particular E_{ii} singularity, so that the SWNTs for each E_{ii} have similar values of d_t, a clear picture emerges for the dependence of ω_D and $\omega_{G'}$ on d_t. The physics behind this averaging is that, by considering a range of chiral angles, the trigonal warping effects associated with the specific nanotube chirality are averaged out and a situation closer to the 2D graphene sheet is obtained. Using the same approach as for the D and G' bands, we averaged the values of $\omega_M^{\pm}$ over all the M band spectra we have available for the E_{33}^S singularity, and similarly for the E_{44}^S singularity, and we then plotted in Fig. B-13 the average values thus obtained for $\hat{\omega}_M^{\pm}$ as a function of the average reciprocal diameter $1/\hat{d}_t$, including the $\omega_M^{\pm}$ values for HOPG at $1/d_t = 0$. A least squares fit to a linear dependence $\hat{\omega}_M^{\pm} = \omega_M^{0\pm} - \beta^{\pm}/\hat{d}_t$ is then made for these three data points for ω_M^{+} and for the corresponding three data points for ω_M^{-}, where the $\omega_M^{0\pm}$ values are chosen as the measured values in HOPG for which $1/d_t \to 0$. The results of the least squares fit to these values yields $\beta^{+} = 18.0\,\mathrm{cm}^{-1}\mathrm{nm}$ and $\beta^{-} = 16.7\,\mathrm{cm}^{-1}\mathrm{nm}$ for the ω_M^{+} and ω_M^{-} features,

respectively. It is interesting that the values for β obtained for these two features are similar to one another, and also to the corresponding value of $16.5\,\mathrm{cm}^{-1}\mathrm{nm}$ for the d_t dependence of the D-band [41, 42]. In addition, we plot in Fig. B-13 the average $\bar{\omega}_M^{\pm}$ values for 51 SWNTs, using the results from Table A.1, and good agreement of these points with the least squares fit in Fig. B-13 is obtained. Similarly, the point labeled E_{22}^M denotes averaged data for 3 isolated metallic SWNTs in resonance with E_{22}^M, and since there are not enough data points available for obtaining a reliable average over chiral angles for E_{22}^M, this point for ω_M^- was not used in the least squares fitting procedure.

The decrease in the average $\omega_M^{\pm}$ with decreasing d_t shown in Fig. B-13 can be associated with an increase in nanotube curvature and a resulting decrease in the vibrational force constants with decreasing d_t. However, for a clear identification of the mode frequencies at the single nanotube level, it is necessary to consider in detail the dependence of $\omega_M^{\pm}$ on chirality, due to the different zone folding effects for phonons and electrons, and to differences in $E_{ii} - E_{\mathrm{laser}}$ for the individual SWNTs.

3.3.4 Resonance issues of SWNTs: from isolated SWNTs to SWNT bundles

It is also interesting to compare the behavior of isolated SWNTs and SWNT bundles. We see that a rich frequency and intensity behavior is observed for the different isolated (n, m) SWNTs, due to the quantum confinement of electrons and phonons in this 1D system. However, when we average over a large number of isolated SWNTs (51 SWNTs in this work), we observe results that are consistent with SWNT bundles, and these results are basically similar to the results observed in the parent material, graphite. From the results presented in Sect. 3.3.3, we see that the assignment of the M band in SWNTs to a combination of the $RBM + G$ bands is not correct, although many average results, [i.e., $\omega_M \sim \omega_{RBM} + \omega_G$ and the splitting $\Delta\omega_M \sim (\omega_{G^+} - \omega_{G^-})$ at $E_{\mathrm{laser}} = 2.41\,\mathrm{eV}$] are in good agreement with this assignment. Also for a few of the isolated SWNTs that we measured, the M feature appears at the same frequency as

the (RBM+G) combination mode at $q \simeq 0$.

The present work shows three new features that are accounted for by the double resonance process: the M^+, M^- and iTOLA features. We further expect that other, yet unassigned, Raman features observed in sp^2 graphite-like materials should be assigned using the double resonance process, considering one, two or more phonon scattering processes (see for example the spectra of Tan et al.[46] on graphite whiskers), and considering not simply the sum of $q = 0$ phonon frequencies, but also difference frequencies in applying the double resonance conditions.

Regarding the low frequency (below $1620\,\mathrm{cm}^{-1}$) second-order combination of modes, we know from the literature[32] that SWNT bundles exhibit two modes that have not yet been assigned. Modes are observed at (1) $\omega_1 = 970\,\mathrm{cm}^{-1}$ and (2) $\omega_2 = 750\,\mathrm{cm}^{-1}$ (for $E_{\mathrm{laser}} = 2.41\,\mathrm{eV}$), and they exhibit opposite frequency dispersions: $\partial\omega_1/\partial E_{\mathrm{laser}} \sim +130\,\mathrm{cm}^{-1}$ and $\partial\omega_2/\partial E_{\mathrm{laser}} \sim -130\,\mathrm{cm}^{-1}$ [32]. These features have not been reported in HOPG, and have only been seen in SWNT bundles. Considering all the branches in the Brillouin zone of 2D graphite, there is no second-order combination of modes that come from either the Γ or the K points that explain this feature. However, if difference frequencies are also considered, an assignment can be made as follows. In this context, we tentatively assign the ω_1 feature in Ref. [32] to the combination of two modes. The first phonon is tentatively assigned as iTA at the Γ point ($|q| = 2|k|$, emission), and the second phonon is assigned to oTA at the K point ($q = 0$, emission). For the feature ω_2 in Ref. [32], we tentatively assign the first phonon to iTA at the Γ point ($|q| \simeq 2|k|$, absorption), and the second phonon to iTA at the K-point ($q \simeq 0$, emission). Alvarez et al. [32] actually give a different assignment to the ω_1 and ω_2 modes, with ω_2 coming from two emission processes and ω_1 coming from one emission and one absorption process based on the observed temperature dependence of ω_1 and ω_2. In making our mode assignments for ω_1 and ω_2 we argue that, in modeling the temperature dependence of ω_1 and ω_2, the Boltzmann factor cannot be strictly considered since the Raman scattering process itself is a source of phonons. As we see below, the assignment we give here predicts quite well the frequency behavior of the ω_1 and ω_2 modes.

Using the set of force constants from Grüneis et al.[37], we calculated the expected ω_1 and ω_2 as well as $\partial\omega_1/\partial E_{\text{laser}}$ and $\partial\omega_2/\partial E_{\text{laser}}$ at $E_{\text{laser}} = 2.41\,\text{eV}$, according to double resonance theory. Since the second phonon is not dispersive ($q \simeq 0$), the dispersion for both ω_1 and ω_2 is given by the slope of the iTA mode, which is opposite for absorption and emission, so that $|\partial\omega_{\text{iTA}}/\partial E_{\text{laser}}| = 127\,\text{cm}^{-1}/\text{eV}$, and the double resonance process gives $\partial\omega_1/\partial E_{\text{laser}} = +127\text{cm}^{-1}/\text{eV}$ and $\partial\omega_2/\partial E_{\text{laser}} = -127\,\text{cm}^{-1}/\text{eV}$, in good agreement with observations [32]. From Ref. [37], the expected frequencies for $E_{\text{laser}} = 2.41\,\text{eV}$ are: $\omega_{\text{iTA}}(\Gamma, |q| = 0.23K) = 305\,\text{cm}^{-1}$, $\omega_{\text{oTA}}(K, q = 0) = 577\,\text{cm}^{-1}$, and $\omega_{\text{iTA}}(K, q = 0) = 1054\,\text{cm}^{-1}$, which gives us $\omega_1 = 882\,\text{cm}^{-1}$ and $\omega_2 = 749\,\text{cm}^{-1}$. Thus, ω_2 is in excellent agreement with experiment, but ω_1 is downshifted by $90\,\text{cm}^{-1}$. This may be due to an inaccuracy in the lower frequency modes near the K point in the force constant model. For example, Raman and infra-red data are plotted for the oTO mode near the K point [47, 48]. According to these data, $\omega_{\text{oTO}}(K, q = 0) \sim 635\,\text{cm}^{-1}$. If we use the oTO instead of the oTA mode value at the K-point, we get $\omega_2 = 940\,\text{cm}^{-1}$, which is $30\,\text{cm}^{-1}$ lower than the observed experimental value.[32] Further investigation of this tentative assignment is needed.

It is interesting to note that a combination of modes involving both the emission and absorption of phonons are commonly observed in molecules such as SO_2 [49, 50]. It is important to stress that, in both cases, the combination modes tentatively assigned to account for the two features observed by Alvarez et al.[32] involves one phonon from close to the Γ point and one from close to the K point. Due to momentum conservation, this combination is not possible in graphite, unless it is a third-order process involving a defect-induced scattering event. In the case of SWNTs, such a process might be possible because of zone folding.

3.4 Concluding Remarks

In this chapter, we present an advance in our understanding of the phonon dispersion relations in graphite-like materials which can be used to interpret experimental second-order Raman spectra taken with different laser excitation energies, thereby

giving more detailed information than in Ref. [8] about the various double resonance Raman processes associated with the Γ point. We expect that other Raman features observed in sp^2 graphite-like materials will in the future be identified in terms of the double resonance process, considering one, two or more phonon scattering processes, and including combinations of both sums and differences of phonon mode frequencies.

From another point of view, the results presented here show that we can use resonance Raman spectroscopy measurements to determine the phonon dispersion relations of graphite and graphite-related materials associated with combination modes and overtones of the sp^2 carbon phonon modes with non-zone-center or zone edge wavevectors in the Brillouin zone of graphite. In this work the M^+, M^- and iTOLA features are identified and can be used to fit phonon dispersion curves in the future [37].

In the case of SWNTs, these second-order overtones and combination bands are found to vary from tube to tube, suggesting a dependence of these spectral features, at the single nanotube level, on tube diameter, chirality, and on E_{ii} values associated with the one-dimensional SWNT electronic and phonon dispersion relations. Furthermore, the experimental results indicate that the resonance condition, i.e., the energy position of E_{laser} with respect to E_{ii}, is also important in the double resonance process in 1D systems. For example, the M^+ feature is only observed for SWNTs with $E_{ii} < E_{\text{laser}}$ and on the basis of the possible phonon scattering processes, we propose a qualitative model to explain this result. Furthermore, we observed modes that can be assigned as the coupling between Γ and K-point phonons. The zone folding of the 2D graphene Brillouin zone into the 1D SWNT Brillouin zone makes it possible to observe the combination of many other phonon features in the interior of the 2D graphite Brillouin zone. The crossing of the possible wave vectors q and k with cutting lines of allowed discrete 1D q and k values for SWNTs needs to be taken into account. Detailed calculations are needed to fully understand these results.

It is also shown that when we average over a large number of isolated SWNTs we observe results that are consistent with SWNT bundles. These results are also basically similar to the results observed in the parent material, graphite, and the

frequency dispersion can be explained by a double resonance theory considering the two-dimensional graphite structure. The results presented here were written up for publication. [51]

Chapter 4

Potential Dependence of Raman-active Vibrational Modes in SWNTs

In this chapter we present a theoretical method of predicting, to within a constant β, the frequency shift in the Raman features of a SWNT material as the Fermi level is changed. The general approach we take is to (1) consider what the joint density of electron states (JDOS) looks like for a given (n,m) SWNT, (2) consider which SWNTs would be resonant with a given laser energy (E_{Laser}), (3) determine - from the diameter distribution of the SWNT material - what the contribution of each SWNT is to the overall JDOS, and (4) determine the total number of electron states that would be filled (or removed) as the Fermi energy is changed. We approximate that the change in frequency of the vibrational modes is linearly dependent on the number of electrons added or removed from the SWNT material.

We then apply this theoretical model to an electrochemical doping experiment performed by Corio *et al.* on SWNT bundles. [52] In that experiment the Raman spectra of semiconducting and metallic SWNTs were collected *in situ* as the Fermi level is changed from 0.0eV to 1.3eV by varying the applied potential of the electrode on which the SWNTs were sitting. By using these data, we calculate the dependence of the G-Band to be $\beta_G = 271\text{cm}^{-1}$ per hole per C-atom, in close agreement to

previous estimates of $\beta_G = 320\text{cm}^{-1}$ per hole per C-atom. [53] Our analysis also predicts observed differences in the behavior of metallic and semiconducting SWNTs. Such an analysis is crucial to understanding how doping effects the vibrational end electronic properties of SWNTs.

4.1 Theoretical

As discussed in Ch. 2, the joint density of states (JDOS) profile for a SWNT is composed of several van Hove singularities (vHs) at energies determined by the diameter of the SWNT and the chirality of the SWNT, by virtue of the trigonal warping effect. The JDOS, $g(E)$, of a semiconducting SWNT is given by Eq. 4.1 [5, 54]:

$$g(E) = \text{Re}\left[\sum_i \frac{a_{C-C}E}{d_t\gamma_0\sqrt{(E - E_{ii} - i\Gamma_J)(E + E_{ii} + i\Gamma_J)}}\right] \tag{4.1}$$

where each term in the summation represents an individual van Hove singularity with a maximum at E_{ii} and a width Γ_J. E_{ii} can be calculated for a given (n,m) SWNT using a tight-binding calculation for graphite along with a with a two-dimensional zone-folding scheme that takes into account the trigonal warping effect. In contrast, Γ_J must be determined experimentally and has been evaluated to be $\sim$ 0.5meV for the E_3 singularity of an isolated semiconducting SWNT on an Si substrate. [54] The additional terms needed to calculate the JDOS are a_{C-C}, the inter-atomic carbon atom distance, γ_0, the tight-binding overlap integral term, and d_t, the diameter of the SWNT. For a metallic SWNT, Eq. 4.1 would include a constant term outside of the summation.

In Fig. B-20, the electron density of states for metallic and semiconducting SWNTs are plotted, showing a van Hove singularity for a semiconducting, (10,8) SWNT and a metallic, (9,9) SWNT. Note the differences between the metallic and semiconducting JDOS profiles. In the case of the (9,9) metallic SWNT, the JDOS is non-zero at energies below the singularity, while the (10,8) semiconducting SWNT has a band-gap with no available electron states below the E_{ii} energy of the singularity. Additionally, the vHs for the (9,9) metallic SWNT is twice as big as the singularity for the (10,8)

semiconducting SWNT. This is because the (9,9) singularity is actually a 'double' singularity, that is, it is the result of two cutting lines equidistant from the K-point of graphite (see Ch. 2). It is important to note that for non-armchair (n≠m) metallic SWNTs, there will be a slight splitting in this 'double' singularity due to the trigonal warping effect.

For a bulk sample of SWNTs, the JDOS picture becomes more complex. As a useful example, we will assume that we have a large number of SWNTs with random (n,m) values and a diameter distribution given by a Gaussian with a mean diameter, $\bar{d} = 1.25$nm and a variance, $\sigma = 0.20$nm. Figure B-18(b) shows the JDOS for the metallic SWNTs in a bulk sample with such a distribution that would be resonant with $E_{Laser} = 1.96$eV. Now the JDOS is no longer given by a single vHs from an individual (n,m) SWNT, but by several different SWNTs with similar diameters but different (n,m) values and slightly different energies for their van Hove singularities. The contribution of each vHs to the overall JDOS is dependent on the diameter, d_t of the particular (n,m) SWNT. Due to the Gaussian distribution of the SWNTs, the van Hove singularities attributed to SWNTs with $d_t \simeq 1.25$nm contribute more to the overall JDOS than SWNTs with more extreme diameters.

The SWNT singularities that would contribute to the JDOS can be determined from the Kataura plot in Fig. B-17 which plots the E_{ii} energy splitting of each SWNT as a function of the nanotube diameter. For a given laser energy, the SWNTs that contribute to the Raman spectrum correspond to the points on this plot where the laser energy and $\bar{d}$ intersect. For $E_{Laser} = 1.96$eV, the Raman spectrum is given by several metallic SWNTs whose E_{11} transition is indicated by the darkly shaded circles in Fig. B-17, and the JDOS of these metallic SWNTs is shown in Fig. B-18(b). Likewise, for $E_{Laser} = 2.54$eV the Raman spectrum is given by semiconducting SWNTs whose E_{33} transition is indicated by the white circles in Fig. B-17, and the JDOS of these semiconducting SWNTs is shown in Fig. B-19(b). Thus, as shown in Figs. B-19(b) and B-18(b), the JDOS for a bulk sample is dependent on which laser energy the sample is being probed with, and the shape of the JDOS is the summation of several van Hove singularities with similar, but not equivalent, E_{ii} values.

Figures B-18(a) and B-19(a) plot the cumulative charge transfer in the metallic and semiconducting SWNTs respectively as the Fermi energy is raised from 0.0eV to a point past the singularities. Note that because semiconducting SWNTs have no available states to fill below their van Hove singularity, the line in Fig. B-19(a) is zero until the the Fermi level is raised past the singularity. In contrast, due to the non-zero JDOS of metallic SWNTs at 0.0eV, the curve in Fig. B-18(a) grows at a linear rate of increase as the Fermi level is increased below the singularity. If the Raman frequency shift for a certain band of the SWNT spectrum is linearly dependent on the occupation of electron states, then as the Fermi energy of the sample is raised, we would expect the frequency of that particular band to shift in a manner similar to the curves in Figs. B-18(a) and B-19(a).

Finally, it is important to note that for semiconducting SWNTs with $d_t \simeq 1.25$nm, the singularity at $\simeq 2.54$eV is the third, E_3 singularity, and there are two singularities below it in the JDOS. Hence, the curve in Fig. B-19(a) should not be identically zero below the E_3 singularity. As a first approximation, however, we neglect the smaller E_1 and E_2 singularities for semiconducting SWNTs and focus on the response of the E_3 singularity as the Fermi level is raised above it.

4.2 Experimental

In this section we apply our theoretical framework developed in the previous section to an experiment performed by Corio *et al* where the Fermi level was raised by means of electrochemical doping and the Raman spectra were taken simultaneously with 2.54eV and 1.96eV laser energies. [52] Our goal is to determine how certain Raman features change in frequency as a response to changing the C-C bond distances by depleting the JDOS for electrons.

4.2.1 Experimental Setup

In the experiment of Corio *et al*, [52] Raman spectra were acquired at room temperature on a Renishaw Raman System 3000 spectrometer equipped with an Olympus

microscope (BTH2) with an 80x objective to focus the laser beam on the sample. For excitation radiation, the 488.0nm (2.54eV) line from an air cooled Ar+ laser and the 632.8nm (1.96eV) line from an air cooled He-Ne laser were used. The experiments were performed under ambient conditions using a back-scattering geometry.

The working electrode was a silver, gold, or platinum electrode with a $0.2cm^2$ geometrical area. A thin film of SWNT bundles was cast on the metal surface from a sonicated dispersion of nanotubes in acetonitrile or isopropyl alcohol. The in-situ Raman spectra were recorded while varying the applied potential in steps of 0.1V, which corresponded to raising the Fermi energy in step of 0.1eV. All the potentials are referred to an Ag/AgCl reference electrode.

The SWNTs used in the work were produced by the electric arc discharge method, using a catalyst with a 1:1 Ni:Co atomic ratio. The diameter distribution of the sample was determined as being $d_t = 1.25 \pm 0.20$nm by analysis of the laser excitation energy dependence of the tangential G-band phonon modes based on Pimenta's method.

4.2.2 Results and Discussion

Metallic SWNTs

Figure B-14 shows the dependence of the Raman spectra taken with $E_{Laser} = 1.96$eV on the applied potential of a SWNT film cast on a Pt electrode in an H_2SO_4 aqueous solution as the potential is scanned between 0.0 and 1.3V. Also presented is the spectrum at 0.0V, obtained after the anodic potential scan was completed. Because of the laser energy and diameter distribution of the sample, these spectra are predominantly produced by metallic SWNTs. By applying positive electrochemical potentials, the electron carrier density of the SWNTs decreases, as the Fermi level is downshifted.

We see in Fig. B-14 that by changing the position of E_{Fermi} in SWNT bundles, we observe frequency and intensity shifts in the the tangential G-Band, the D-Band and the G'-Band, while the RBM peak remains primarily at the same frequency, but changes in intensity. The frequency dependence on E_{Fermi} of the G-Band, D-Band and G'-Band is non-linear and different for each feature. Plots of the behavior of

these three Raman features are shown in Fig. B-16. As can be seen in this figure, the nature of the frequency dependence on E_{Fermi} is similar to the shape of the cumulative charge transfer curve for metallic SWNTs shown in Fig. B-18(a). Thus by fitting the curve in Fig. B-18(a) to the frequency response plot in Fig. B-16, we can roughly calculate the dependence of the G, D, and G'-Bands on charge transfer for metallic SWNTs. Using this method we calculate the dependencies to be β = 271, 224, and 460cm^{-1} per hole per C-atom for the G, D, and G'-Bands respectively for metallic SWNTs. The calculated value of β_G = 271cm^{-1} per hole per C-atom is in close agreement to the previously determined experimental value of β_G = 320cm^{-1}, evaluated by Sumanasekara *et al* for semiconducting SWNTs [53].

It is important to note that, although all three of these Raman features behave roughly the same way, there are some noticeable differences. First, although the frequency dependence of the D-Band is roughly one half that of it's first overtone, the G'-Band, the D-Band does not shift in frequency until E_{Fermi} is raised to 0.8eV. In contrast, the G'-Band frequency exhibits a linear growth pattern even for small shifts in the Fermi energy. Additionally, the steep frequency shift for all three of these modes is observed to begin at different E_{Fermi}. In the case of both the D and G-Band, the major shift in frequency begins at 0.8eV, but the G-Band frequency appears to stop changing after E_{Fermi} = 1.0eV, while the D-Band frequency continues to change up to E_{Fermi} = 1.2eV. The G'-Band begins to shift most dramatically in frequency when E_{Fermi} = 1.0eV and continues this behavior through E_{Fermi} = 1.3eV. Although these differences are difficult to understand exactly, they do lend some understanding to the non-linear dependence of each of these modes on the occupation or depletion of electron states.

Semiconducting SWNTs

Figure B-15 shows the dependence of the Raman spectra taken with E_{Laser} = 2.54eV on SWNT bundles in an H_2SO_4 media for positive applied potentials up to 1.4 V. Due to the diameter distribution of the sample, E_{Laser} = 2.54eV should be resonant with semiconducting SWNTs as understood from the Kataura plot in Fig. B-17. As

in the case with metallic SWNTs, by applying positive electrochemical potentials, the electron carrier density of the SWNTs decreases as the Fermi level is downshifted.

We observe in Fig. B-15 that as the applied voltage is raised from 0.0 V to 1.4 V, the D, G and G'-Bands all exhibit upward frequency shifts and losses in intensity similar to those observed for metallic SWNTs in Fig. B-14. In Fig. B-16 (white squares) we plot the positions of the Raman shifts for these modes at different E_{Fermi}. Through these points, we plot the theoretical cumulative change transfer curve calculated Fig. B-19(a), using the same constants evaluated for metallic SWNTs to determine the frequency dependence on charge transfer (β). As was the case for metallic SWNTs, the change in frequency shift of the Raman modes at each E_{Fermi} seem to closely follow the theoretical predictions for the cumulative charge transfer, as E_{Fermi} is raised or lowered. Specifically, we note that for semiconducting SWNTs, there is no major change in frequency in any of the Raman modes until E_{Fermi} is raised past the expected position of the E_3 van Hove singularity, which reflects the existence of a band gap associated with the third subband.

In Fig. B-16, we plot the theoretical Raman frequency shift line for semiconducting SWNTs using constants (β) evaluated for metallic SWNTs largely because of the unaccounted for E_1 and E_2 singularities that exist in the semiconducting JDOS. The Γ_J factor in Eq. 4.1 for E_1 and E_2 is yet to be determined experimentally as it was for E_3, [54] and hence it is difficult to predict what the cumulative charge transfer would be as E_{Fermi} is raised past E_1 and E_2 for semiconducting SWNTs. Thus, the β-constants evaluated for metallic SWNTs are expected to be more accurate than the β-constants that would be determined from the semiconducting SWNTs. However, it should be noted that there are effects in Fig. B-16 (with E_{Laser}=2.54eV) that could be attributed to the E_1 and E_2 singularities, specifically, the frequency shift in the D-Band, that occurs at E_{Fermi}=0.6eV and the shift in the G-Band at E_{Fermi}=0.4eV.

Details

Figures B-14 and B-15 show that at a potential of 1.3 V, the Raman spectrum of the SWNT sample resembles the spectra of disordered carbon, which could suggest

the onset of electrochemical destruction of the SWNT. However, when the applied potential returns to 0.0 V, the characteristic SWNT spectral features are restored. This behavior can be understood by considering that, at 1.3 V, electrons have been removed from the E_1^M and E_3^S van Hove singularities (vHs) of the valence band in the metallic and semiconducting SWNTs in the sample. When the Fermi level has been moved through a particular vHs, the initial state of the electrons in the interband transition are no longer occupied. Since resonance must be with a transition from an occupied to an empty state, the resonance Raman condition is no longer satisfied when E_{Fermi} passes through the vHS in the valence band that was resonant with E_{Laser}. The results in Figs. B-14 and B-15 are consistent with the removal of electrons from the valence band van Hove singularities responsible for the E_{11}^M and E_{33}^S transitions as the potential is increased from 0.0 to 1.3V. For metallic SWNTs, because there is a non-zero term in the JDOS below the E_1^M van Hove singularity, there is a change in the Raman intensity well before E_{Fermi}=E_1^M, as is clearly observed in the G'-Band in Fig. B-14. After E_{Fermi} has fallen below E_1^M and E_3^S for all the SWNTs in the sample, the resonance condition with E_{Laser} is no longer satisfied and the intensity of the observed Raman features drops off dramatically. Figures B-14 and B-15 show that the effect is reversible, i.e., when the electronic density of the SWNTs is reestablished by applying a more negative potential, the characteristic spectrum of SWNTs is seen again. Note, however, that although the intensities and frequencies of the major Raman features are restored after E_{Fermi} is brought back to 0.0eV, the intensity of the D-Band has increased relative to the other Raman features. Since the intensity of the D-Band is related to the number of defects in a SWNT, this change in D-Band intensity indicates that the electrochemical processing has introduced disorder to the SWNT material.

When considering why the frequency shifts in the Raman spectrum occur, there are three effects that must be considered. First, the charge transfer process induces a softening or hardening of the C-C bond. This affects the frequencies of the vibrational modes and subsequently changes the resonance condition, and therefore also affects the absolute intensities. Second, the charge transfer process changes the filling of

electronic states, and therefore changes the resonance condition with the exciting laser energy, since the resonance must be with a transition from an occupied to an empty state. This mechanism significantly changes which electronic transitions are taking place, and therefore changes the frequency of doubly resonant Raman modes such as the D-Band and G'-Band (see Ch. 2). Lastly, it should be considered that there is also a small electrochemical-induced perturbation to the energy levels themselves, which also affects the resonance condition. Although the latter two factors probably have a much weaker effect on the frequency of the Raman modes than the softening and hardening of the C-C bond, they must be considered if one is trying to make an accurate evaluation of β.

4.3 Concluding Remarks

In this chapter a model is introduced to calculate the frequency dependence of the Raman-active SWNT vibrational modes on the Fermi energy of a SWNT material. As a first approximation, it is assumed that the frequency of each vibrational mode is linearly dependent on the addition or depletion of electrons from the SWNT material - which is expected to change the length of the C-C bonds. Thus, by making a determination of the JDOS of a SWNT material, and by summing all the possible states up to a certain E_{Fermi}, we are able to calculate, up to a factor β, the frequency dependence of the D, G and G'-Bands on E_{Fermi}. To evaluate this factor β for each mode, we compare our theoretical predictions to the data obtained in an experiment by Corio *et al.* , where the Fermi energy of a SWNT material was raised by electrochemical doping as the Raman spectra were being simultaneously obtained *in-situ* with two laser energies to analyze metallic and semiconducting SWNTs separately.

By using this method we determine that $\beta_G = 224$, $\beta_G = 271$ and $\beta_{G'} = 460\text{cm}^{-1}$ per hole per C-atom for metallic SWNTs with $d_t \simeq 1.25 \pm 0.20\text{nm}$. These results correspond well to a previous estimate of $\beta_G = 320\text{cm}^{-1}$ per hole per C-atom for semiconducting SWNTs with $d_t \simeq 1.35\text{nm}$ [53]. For semiconducting SWNTs, the theoretical model proposed in this chapter neglects the contributions to the JDOS of

the E_1 and E_2 singularities, and hence is only able to qualitatively describe observed changes in the Raman spectra. This work was written up for publication. [52]

Accurate evaluations of β would allow the amount of charge transfer in a SWNT material to be determined precisely using spectroscopic techniques. Such an ability is important for SWNT experiments where charge transfer may occur, for example, by way of substrate effects on SWNTs or chemical doping of SWNTs. The natural development of this work is to use this theory to analyze the Raman spectra of isolated SWNTs as the Fermi energy is changed.

Chapter 5

Conclusions

In this thesis, two experiments were analyzed that use resonance Raman spectroscopy to characterize the vibrational properties of single-walled carbon nanotubes. In chapter 3, we present an analysis of second-order Raman modes observed at $\sim$1750cm^{-1} (M-band) and $\sim$1950cm^{-1} (iTOLA) for sp^2 graphite-like materials, including highly oriented pyrolytic graphite (HOPG), SWNT bundles, and isolated SWNTs. By applying double resonance Raman theory to spectra taken from HOPG and SWNT bundles with varying E_{laser}, we have determined the origin of these features and have fit them to the phonon dispersion relations of graphite. On the isolated SWNT level, it was determined that the appearance of the M^+ feature for a particular SWNT is contingent on $E_{ii} < E_{\text{laser}}$, however, exact explanations of the appearance and frequency of these features remains forthcoming. The next step of this analysis is to obtain the Raman spectra of a single isolated SWNT with several different laser energies. With such data, the phonon dispersion relations for an isolated SWNT could be fitted, and a more exact understanding of double resonance features of SWNTs could be achieved. Additionally, theoretical calculations can now be carried out using the recently derived electron-phonon matrix elements [55] to predict the Raman spectra of SWNTs. Such calculations will show which double resonance processes are expected to have a small intensity, and which are unlikely to occur, hence allowing us to make better assignments of observed double resonance Raman features.

In chapter 4, a model is introduced to calculate the frequency dependence of the

Raman-active SWNT vibrational modes on the Fermi energy of a SWNT material. The frequency of these modes are expected to shift due to changes in length of the C-C bonds caused by the addition or depletion of electrons. Our theoretical model presented here assumes that the shift of each Raman feature is linearly related to the Fermi energy through some constant, β, which we attempt to calculate by analyzing Raman spectra collected *in-situ* as the Fermi energy of a SWNT material is raised upon application of an external voltage to the electrode on which the SWNT material is sitting. The evaluations of β we obtained for metallic SWNTs correspond well with previous determinations using similar methods. [53] For semiconducting SWNTs, however, Raman features in the observed spectra fail to shift in frequency at expected Fermi energies (i.e. at the E_1 and E_2 singularities). Additionally, separate Raman features - D-band, G-band and G'-band - tend to behave differently as the Fermi energy changes, providing information regarding the non-linear dependence of these features. To explain these differences, the natural development of this work is to analyze the Raman spectra of isolated SWNTs as the Fermi energy (applied voltage) is changed.

Appendix A

Tables

Table A.1: Frequencies ω_M^+ and ω_M^-, frequency difference $\Delta\omega_M$ between ω_M^+ and ω_M^- and the (averaged) diameters d_t for the spectra shown in Fig. B-7.

	HOPG	SWNTs		
		bundle	(15,7)	avg. SWNTs[†]
ω_M^-	1754	1732	1731	1744
ω_M^+	1775	1755	1751	1766
$\Delta\omega_M$	21	23	20	22
d_t	∞	1.55*	1.52	1.6

*1.55 nm denotes the averaged diameter distribution of the SWNTs resonant with $E_{\text{laser}} = 2.41\,\text{eV}$, deduced from the RBM feature in the SWNT bundle sample [30].
[†]Average over 51 isolated SWNTs (see text).

Appendix B

Figures

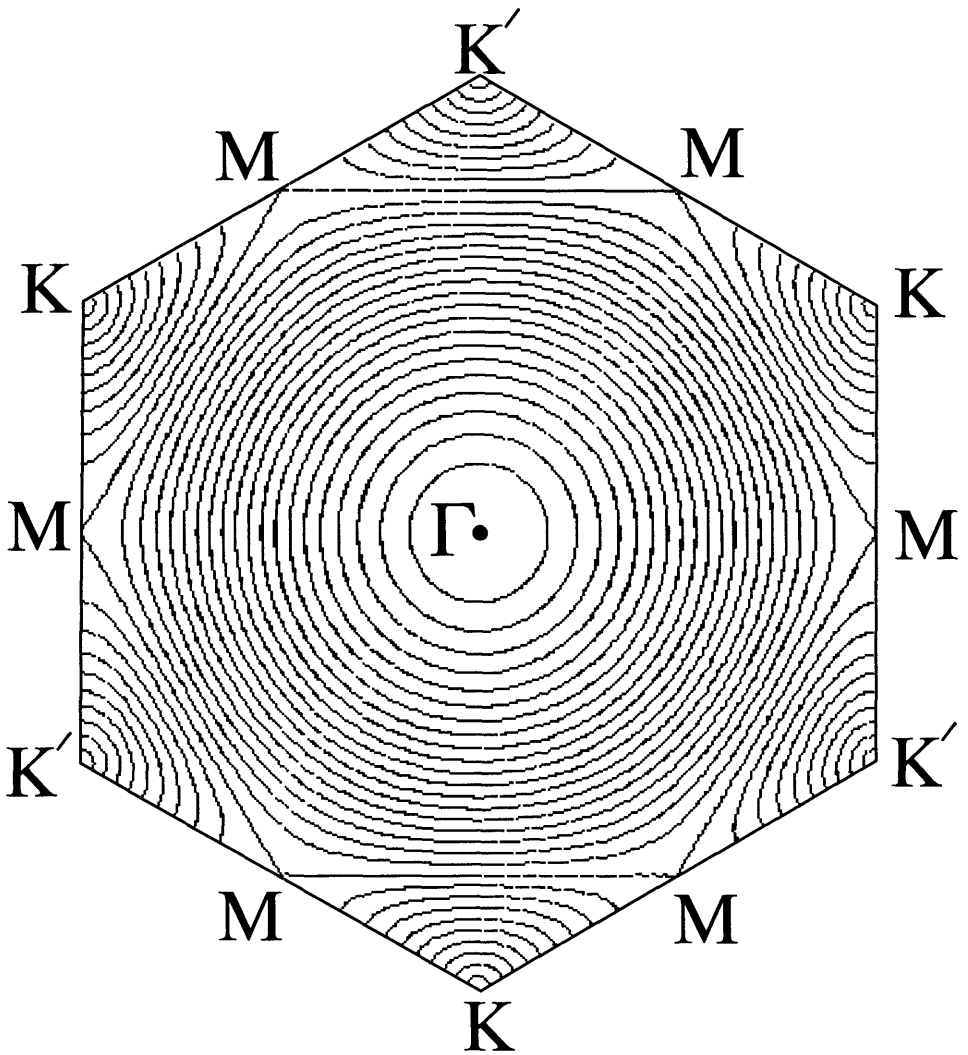

Figure B-1: Equi-energy contours for the π^* band of 2D graphite. The Γ, **K**, and **M** points indicate the high symmetry points of an hexagonal graphite sheet. In this figure, the energy at the Γ point is greatest while the energy at the **K**-point is lowest.

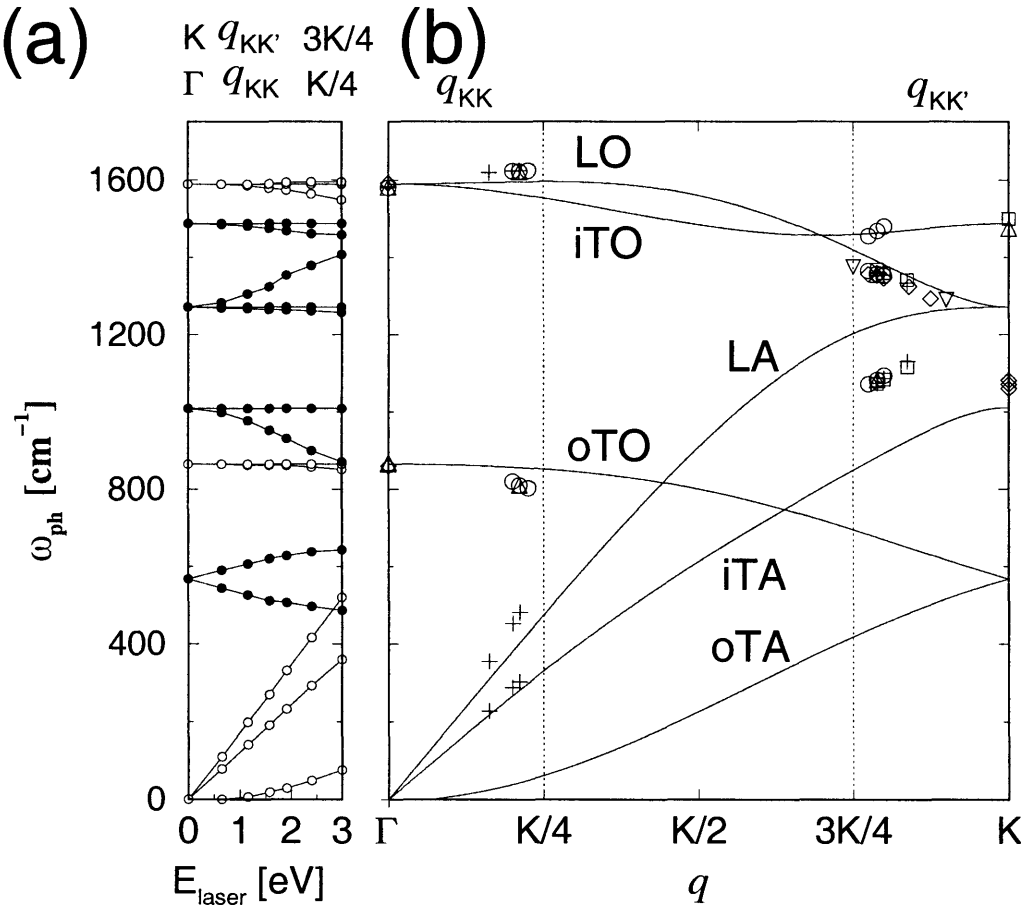

Figure B-2: (a)- The calculated Raman frequencies for carbon materials as a function of incident laser energy, E_{laser} for the $q \sim 2k$ double resonance condition. (b)- The 6 phonon dispersion curves for 2-D graphite. Plotted on top of these curves are symbols which correspond to experimental Raman observations of different carbon materials. These symbols have been placed according to double resonance theory. [8] "○" - pyrolytic graphite(PG) Ref. [56], box - C ion implanted HOPG(C-HOPG) Ref. [57], triangle - highly ordered pyrolytic graphite (HOPG) Refs. [56, 58] diamond - single walled carbon nanotubes(SWNT) Refs. [27, 32, 59], "+" - graphite whisker (GW) Ref. [46]. "▽" - micro-crystalline graphite (MG) Ref. [21].

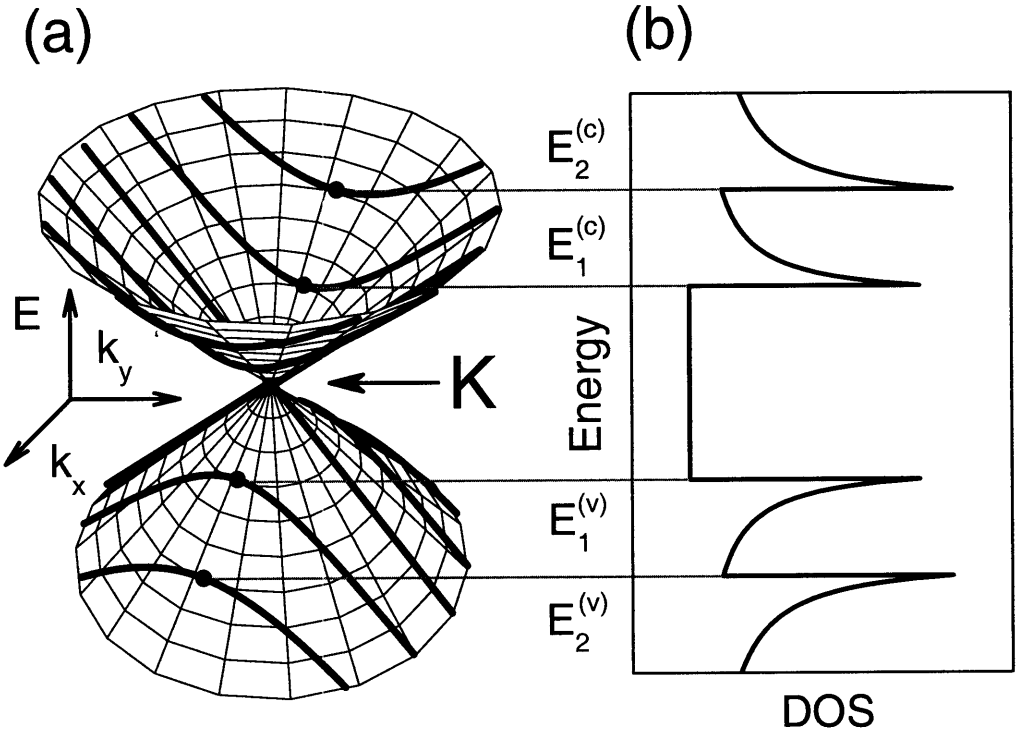

Figure B-3: (a) The energy vs. momentum contours for the valence and conduction bands of 2D graphite near the **K**-point. The cutting lines represent the dispersion relations for a 1-D SWNT. Each cutting line gives rise to a different van Hove singularity in the density of electronic states for the SWNT, shown in (b). [8]

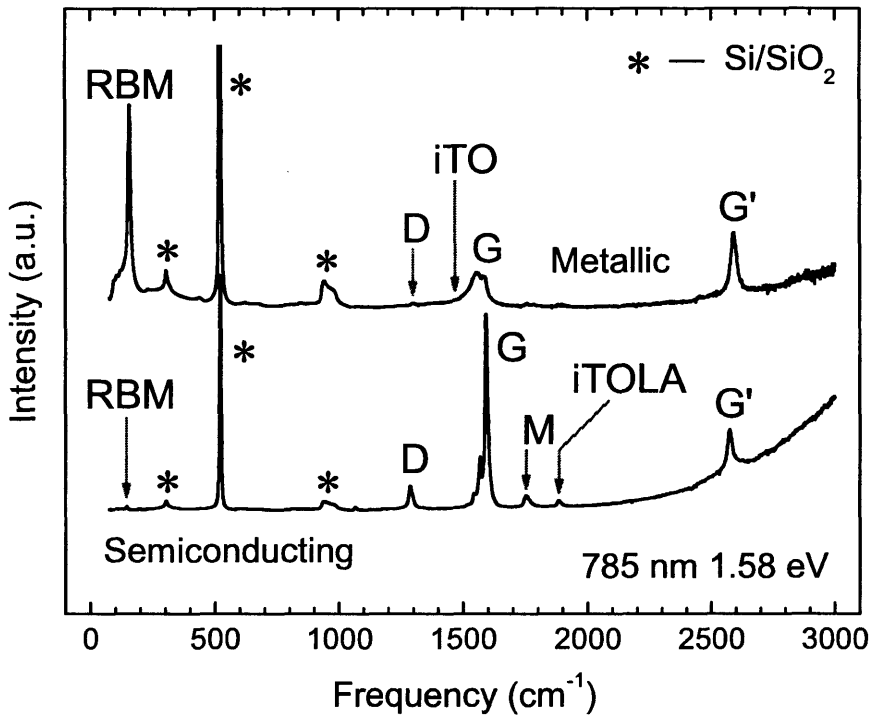

Figure B-4: Raman spectra from isolated metallic (top) and semiconducting (bottom) SWNTs taken with $E_{laser} = 1.58$ eV (785 nm). The radial breathing mode (RBM) and G-band correspond to first-order Raman processes. The D-band, G'-band, iTOLA mode and M-band correspond to double resonance features, of which, the G'-band, iTOLA mode, and M-band are two-phonon processes, while the D-band is a single phonon process. '*' denotes features of the Si Raman spectra which are produced by the Si/SiO_2 substrate. [9]

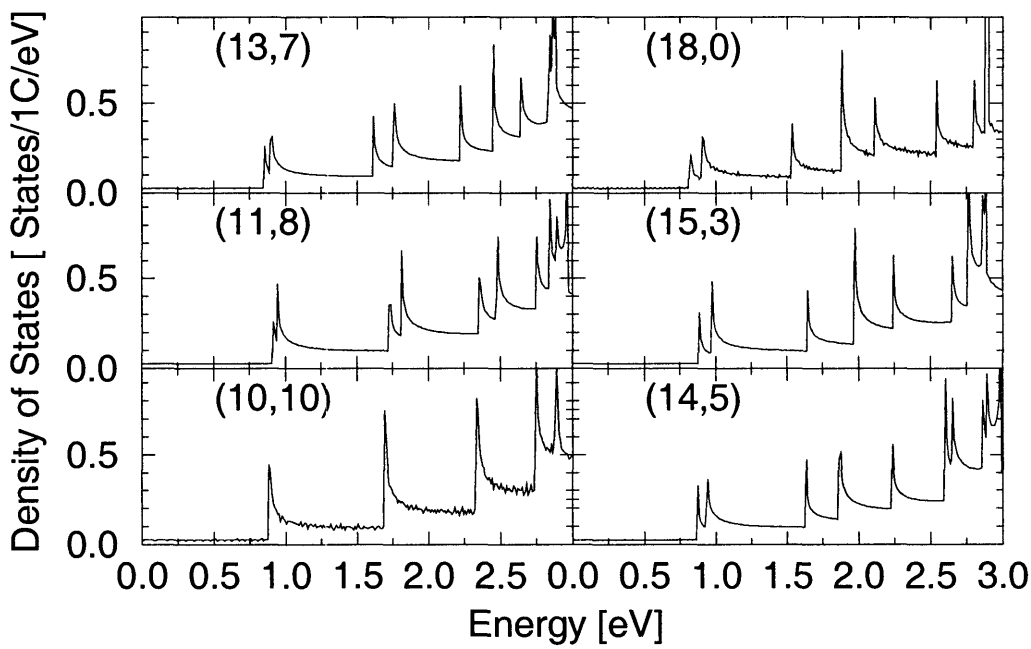

Figure B-5: Density of electronic states (JDOS) for six metallic SWNTs with approximately the same diameter. Note the a the positions for the van Hove singularities differ, and that in some cases a large singularity will be split into two smaller singularities with slightly different energies. This splitting is negligible for the armchair (10,10) SWNT, and greatest for the zig-zag (18,0) SWNT.

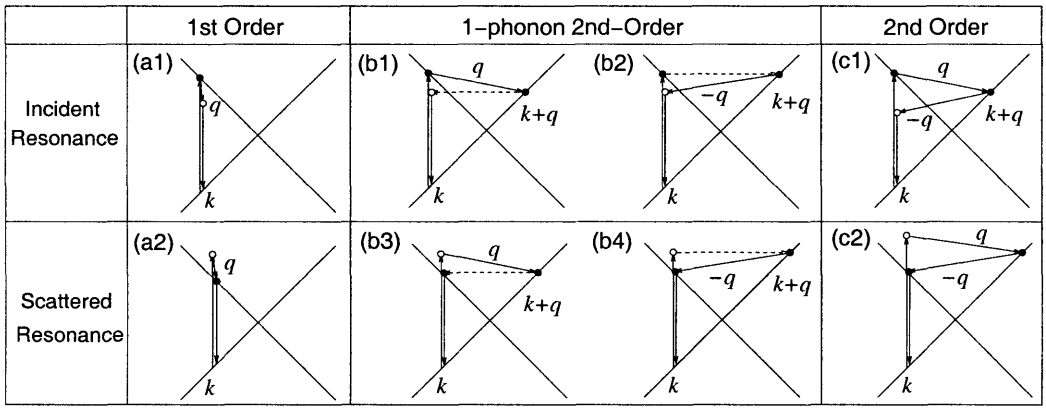

Figure B-6: First-order (a1, a2), one-phonon second-order (b1-b4) and two-phonon second order (c1, c2) resonance Raman processes. Cases where the incident photon is resonant are shown on the top, while cases where the scattered photon is incident are shown on the bottom. For one-phonon double resonance processes, one of the scattering events is produced by defects, as is represented by the dashed line. Solid circles represent resonance points. [9]

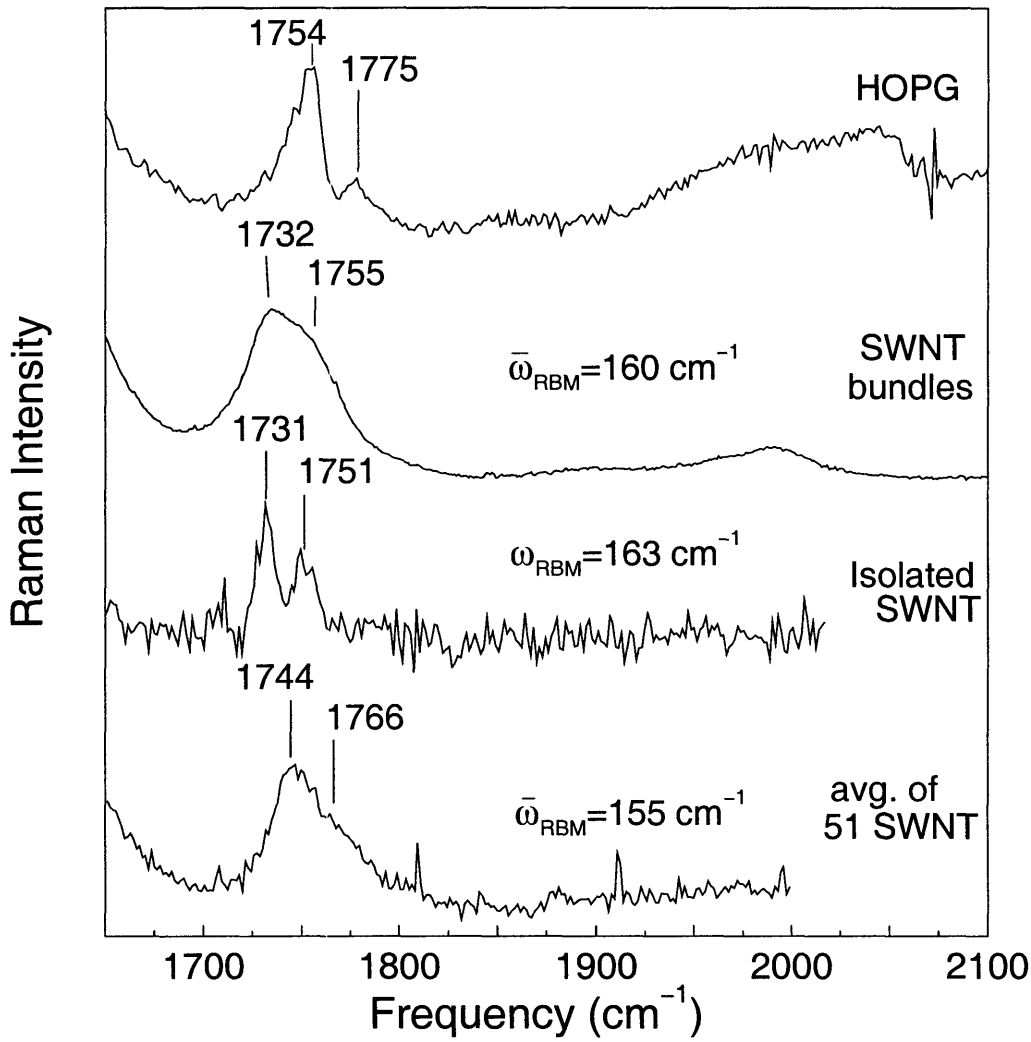

Figure B-7: Raman spectra from HOPG, SWNT bundles, an isolated SWNT, and an average over 51 isolated SWNTs, where the average is taken by summing the 51 spectra, all normalized to a common feature in the Raman spectrum of the silicon substrate. All of these spectra were excited at laser energy $E_{\text{laser}} = 2.41\,\text{eV}$. The frequencies of some peaks are indicated in cm^{-1}, and $\overline{\omega}_{\text{RBM}}$ denotes the average radial breathing mode frequency for the SWNT bundle and for the sum of the 51 spectra for isolated SWNTs.

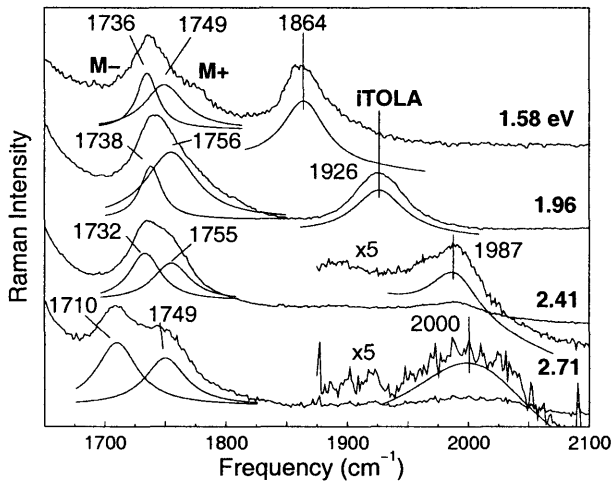

Figure B-8: Lorentzian fits of the Raman spectra taken at several E_{laser} values for the M feature near $1750\,\text{cm}^{-1}$ and the highly dispersive iTOLA feature observed at $1950\,\text{cm}^{-1}$ in SWNT bundles, taken from Brown et al. [30]. Peak frequencies (cm^{-1}) and E_{laser} values (eV) are displayed.

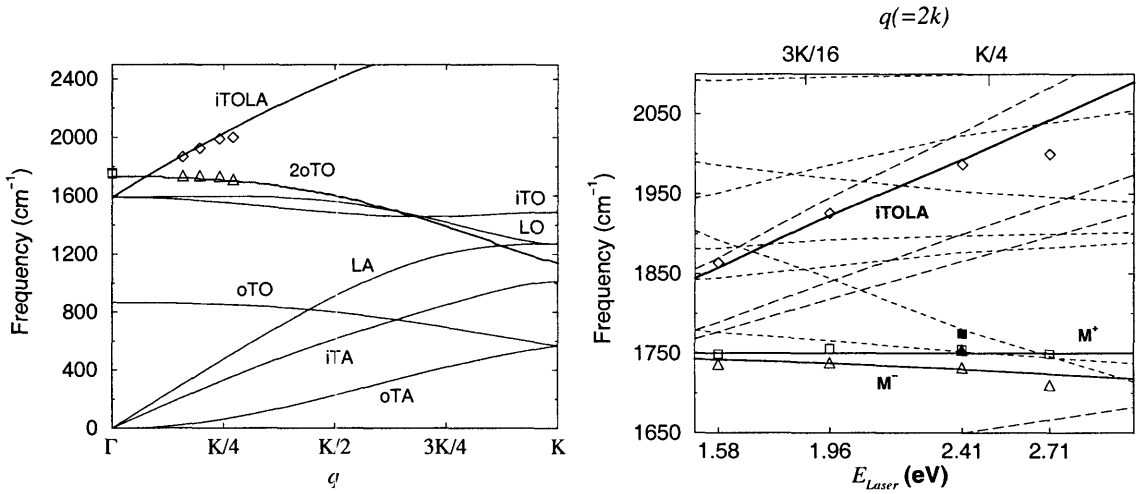

Figure B-9: (a) The phonon dispersion curves for graphite from the Γ-point to the K-point from Ref. [8]. Also plotted are the predicted dispersion relations and experimental points for the second-order overtone of the out-of-plane optical (oTO) mode (related to the $M^{\pm}$ bands) and for the second-order combination iTO+LA of the in-plane transverse optical (iTO) and longitudinal acoustic (LA) modes (related to the iTOLA band). (b) ω_M^-, ω_M^+ and ω_{iTOLA} frequencies vs. E_{laser} (lower scale) for the M bands and the iTOLA band. This figure corresponds to an expanded scale for (a). The corresponding $|q| \simeq 2|k|$ values for M^- and iTOLA are plotted on the upper scale (the upper scale does not apply to the M^+ mode). The experimental results from SWNT bundles taken from Fig. B-8 are represented by: ω_M^- (△), ω_M^+ (□), iTOLA (◇). The solid curves represent the predicted frequencies of $\omega_M^{\pm}$ vs. E_{laser} upshifted by $20\,\mathrm{cm}^{-1}$, and the dark solid curve shows the predicted frequencies of ω_{iTOLA} vs. E_{laser} (unshifted). The dashed lines show all the other possible predicted combination and overtone modes in graphite associated with the K-point, while the long dashed lines represent predicted combination and overtone modes from the Γ-point, according to double resonance theory [8].

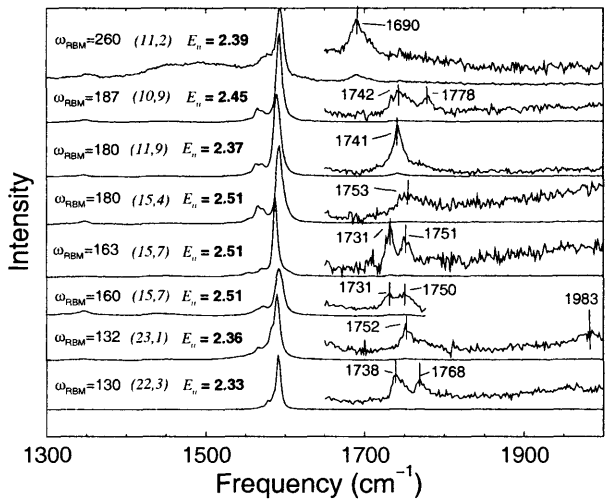

Figure B-10: Raman spectra taken with $E_{\text{laser}} = 2.41\,\text{eV}$ from several isolated SWNTs which clearly show the M band. For each tube the tentatively assigned (n, m) indices and the observed ω_{RBM} and $\omega_M^{\pm}$ frequencies (cm^{-1}) are also displayed. The unusual G band observed for the upper trace $(11, 2)$ is related to the very small (below 1.0 nm) tube diameter (see Refs. [45] and [39]).

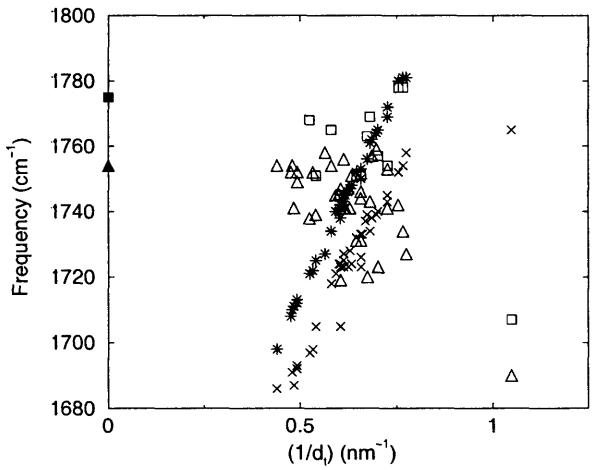

Figure B-11: Experimental M-band frequency vs. $(1/d_t)$ data points are shown as open symbols. The $\square$ are used for ω_M^+ when two features are observed and $\triangle$ are used for ω_M^-. The points denoted by * indicate the frequency predicted for the $q \simeq 0$ combination mode $\omega_G^+ + \omega_{\mathrm{RBM}}$, while the predicted $\omega_G^- + \omega_{\mathrm{RBM}}$ at $q \simeq 0$ are denoted by $\times$ (see text). The observed ω_M^+ and ω_M^- data points for HOPG at $E_{\mathrm{laser}} = 2.41\,\mathrm{eV}$ are denoted by a filled square and a filled triangle at $(1/d_t) = 0$.

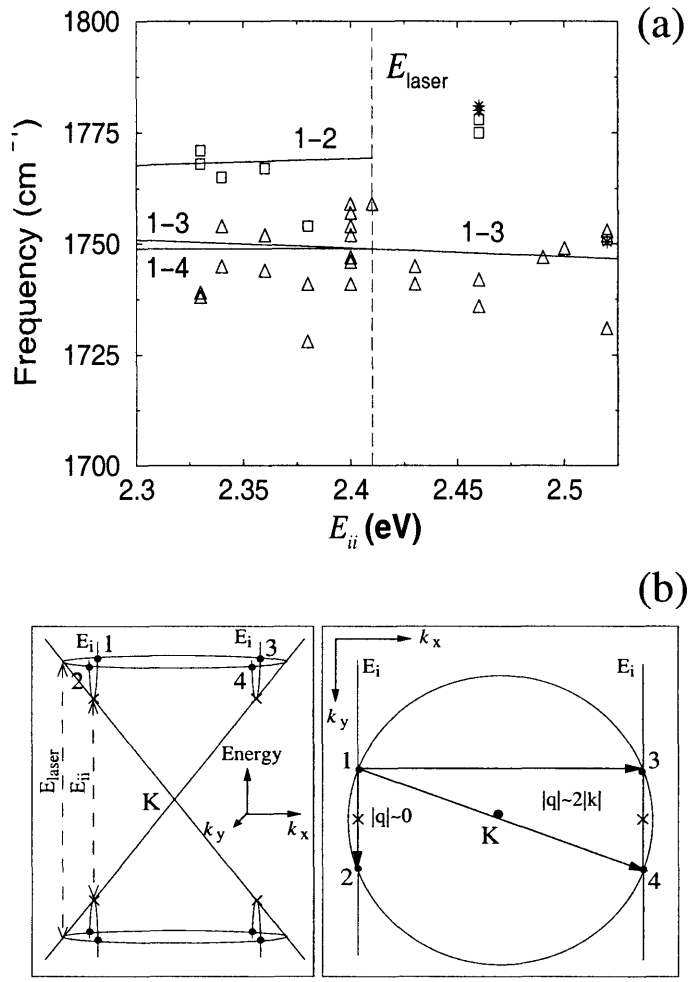

Figure B-12: (a) Frequencies for $\omega_M^-(\triangle)$ and $\omega_M^+(\square)$ observed with $E_{\text{laser}} = 2.41\,\text{eV}$ vs. the energy of the van Hove singularity in the joint density of states E_{ii} for isolated SWNTs. The solid curves are predictions for the frequencies expected from the model in (b). (b) Schematic model to explain the observation of one or two M peaks in the Raman spectra for isolated SWNTs (see text).

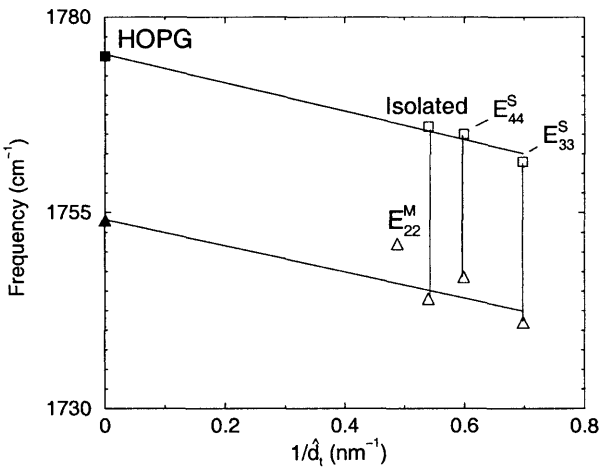

Figure B-13: Plot of the experimental frequencies ω_M^+ and ω_M^- averaged over the E_{33}^S singularity and over the E_{44}^S singularity in the joint density of states of individual SWNTs vs. their average $1/\hat{d}_t$ values. Also included are the corresponding experimental points for HOPG ($1/d_t \to 0$). A least square fit of $\omega_M^\pm$ to these data points yields $\hat{\omega}_M^+ = 1775 - 18.0/\hat{d}_t$ and $\hat{\omega}_M^- = 1754 - 16.7/\hat{d}_t$. The data points labeled "isolated" are for an average of $\omega_M^\pm$ for 51 isolated nanotubes (see text). The data point E_{22}^M represents an average of ω_M^- for 3 metallic SWNTs corresponding to the E_{22}^M singularity (see text).

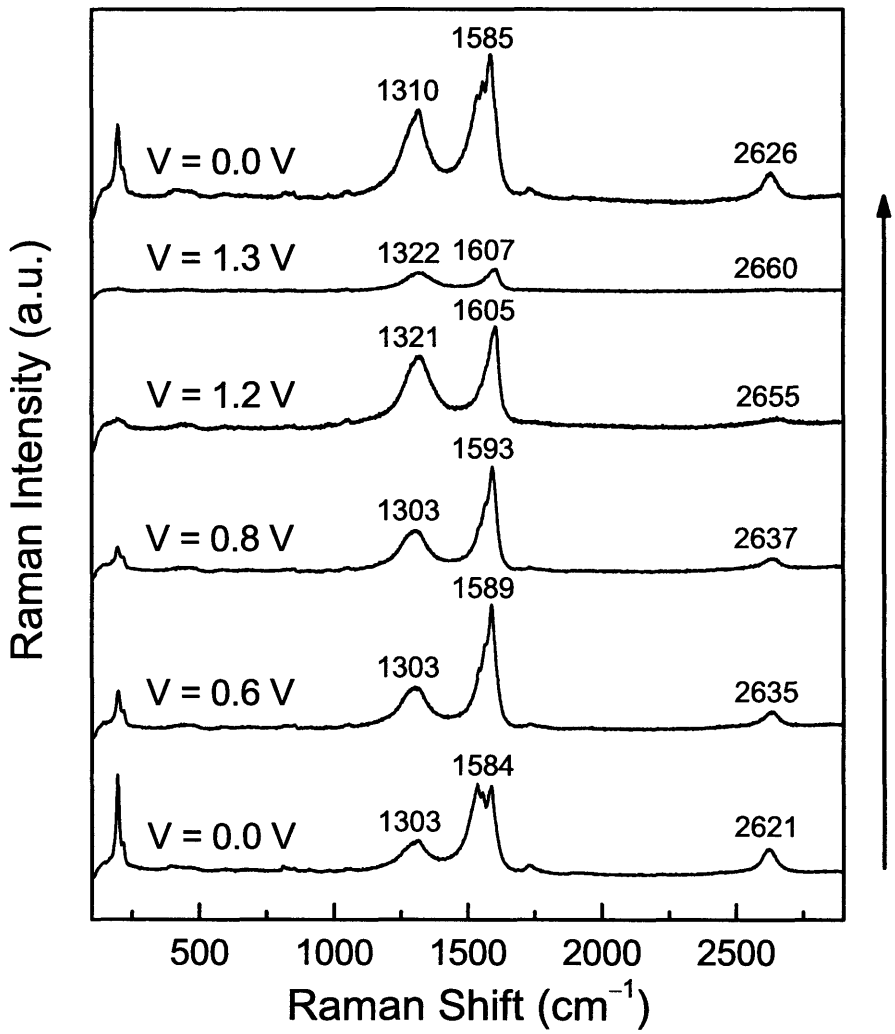

Figure B-14: *In situ* Raman spectra of a SWNT film cast on a platinum surface in H_2SO_4 0.5 M aqueous solution obtained at the indicated applied potentials. E_{Laser}=1.96eV (metallic SWNTs).

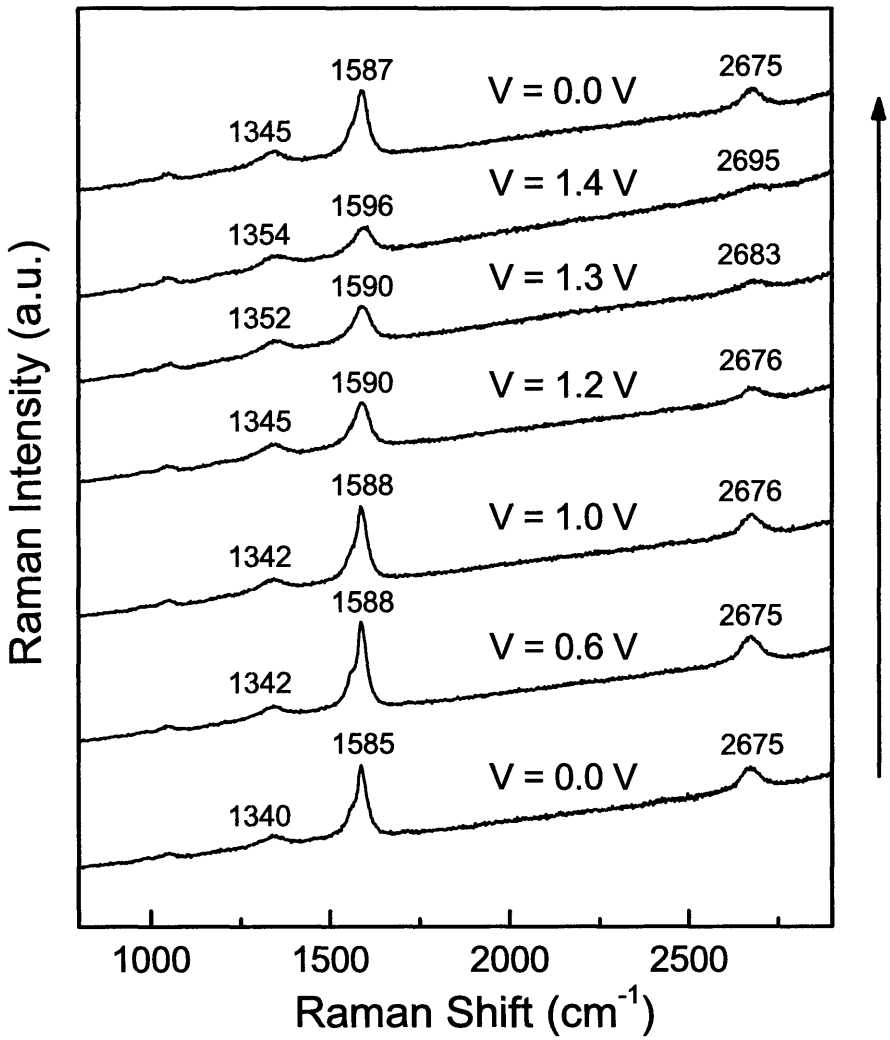

Figure B-15: *In situ* Raman spectra of a SWNT film cast on a platinum surface in H_2SO_4 0.5 M aqueous solution obtained at the indicated applied potentials. E_{Laser}=2.54eV. (semiconducting SWNTs)

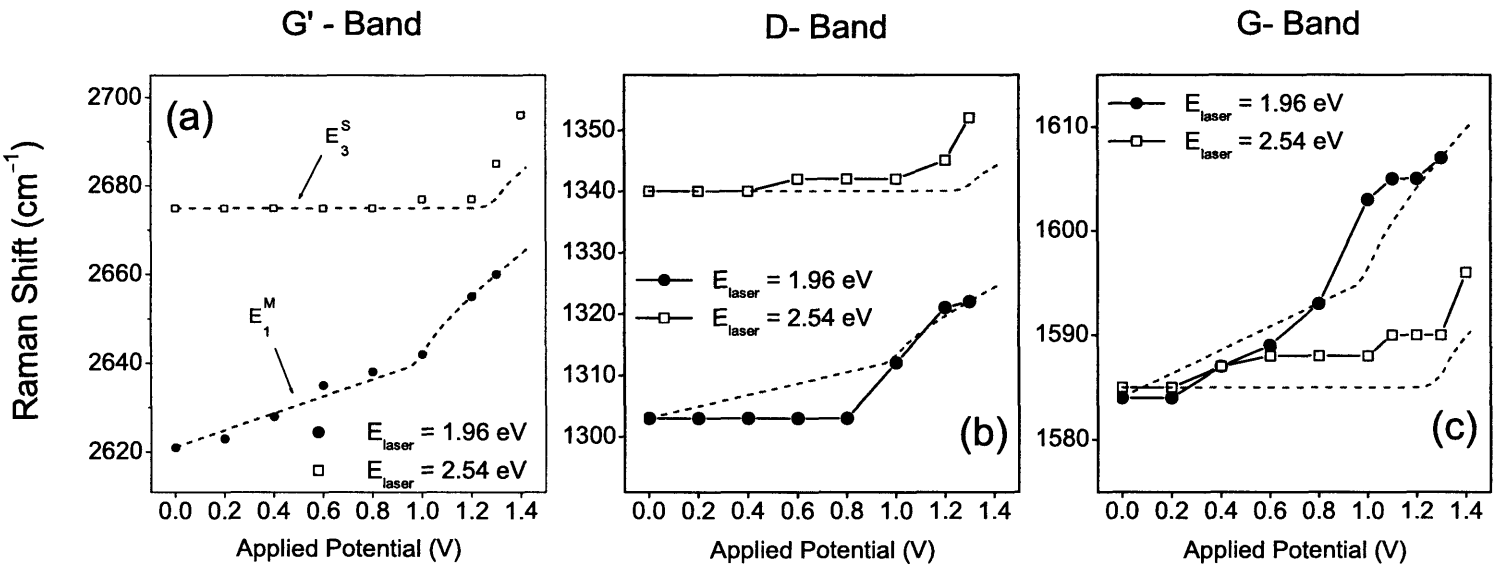

Figure B-16: Raman shift of (a) the G'-band, (b) the D-band, and (c) the tangential G-band for a SWNT film on a platinum surface in H_2SO_4 0.5 M aqueous solution obtained at the indicated applied potentials for E_{Laser}=1.96eV (metallic SWNTs, •) and E_{Laser}=2.54eV (semiconducting SWNTs, □). Shown by dotted lines are the theoretical curves of the calculated cumulative charge transfer in the SWNT density of states, multiplied by some differ factor, β, for each vibrational mode. In this figure β_D=224, β_G=271, and $\beta_{G'}$=460cm^{-1} per hole per C-atom.

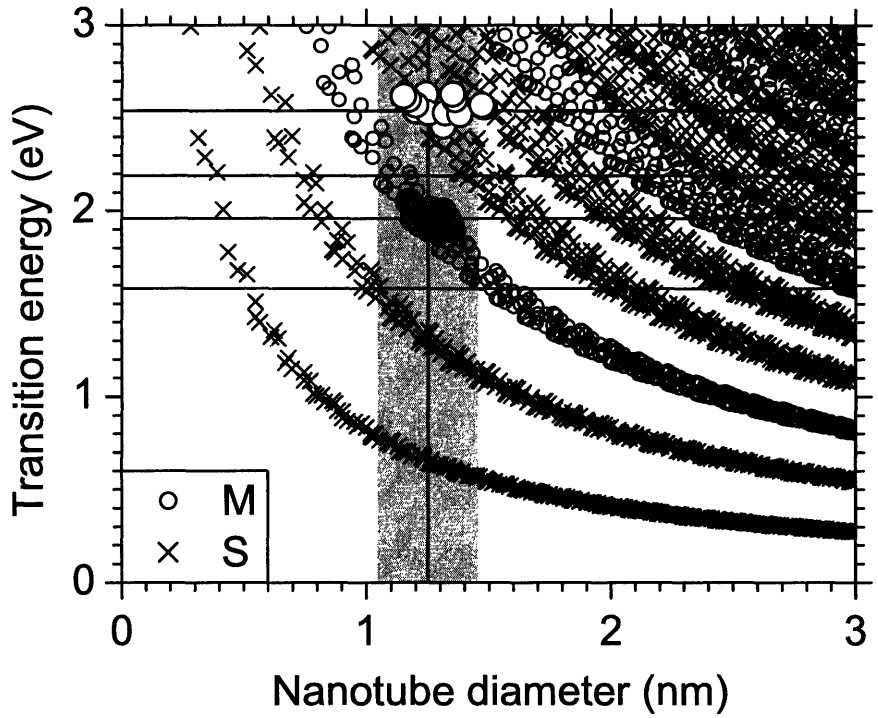

Figure B-17: Electronic transition energy *vs.* tube diameter obtained by the zone-folding scheme [5] from the Slater–Koster model [60] with the transfer integral γ_0=2.89 eV. [12] Dots and crosses denote metallic and semiconducting SWNTs, respectively. The vertical stripe gives the diameter distribution for SWNT sample used by Corio *et al*, d_t=1.25±0.20 nm. Horizontal lines show E_{Laser}=2.54 and 1.96 eV (488.0 and 632.8 nm, respectively). The gray and white large circles indicate metallic and semiconducting SWNTs that would be resonant with the given laser energies.

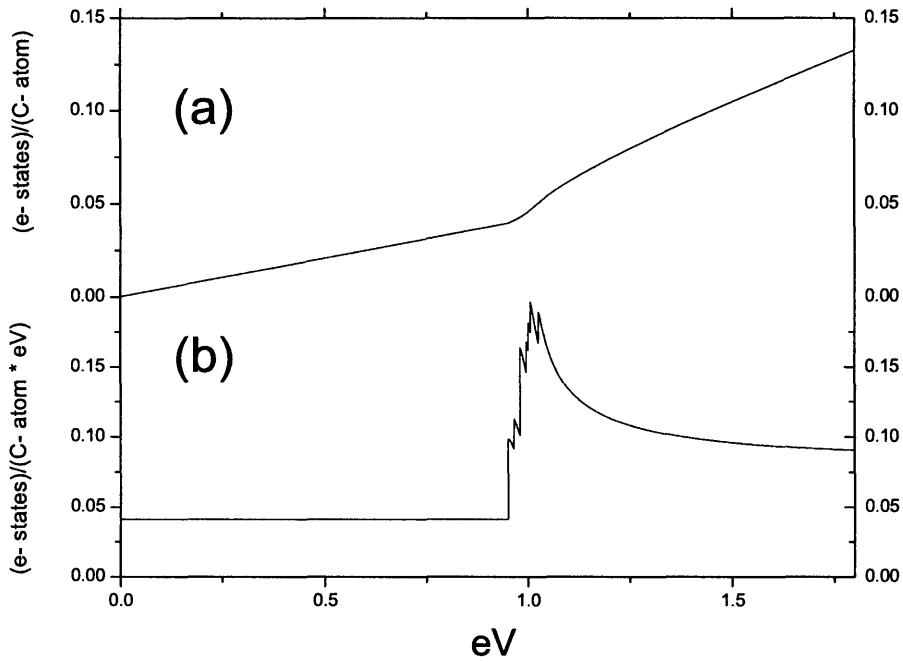

Figure B-18: (b) The total JDOS for all metallic SWNTs that would be resonant with E_{Laser}=1.96eV from a diameter distribution of d=1.25±0.20 nm.
(a) The cumulative number of electron states filled or depleted as the JDOS (b) is integrated from 0.0eV to E_{Fermi}.

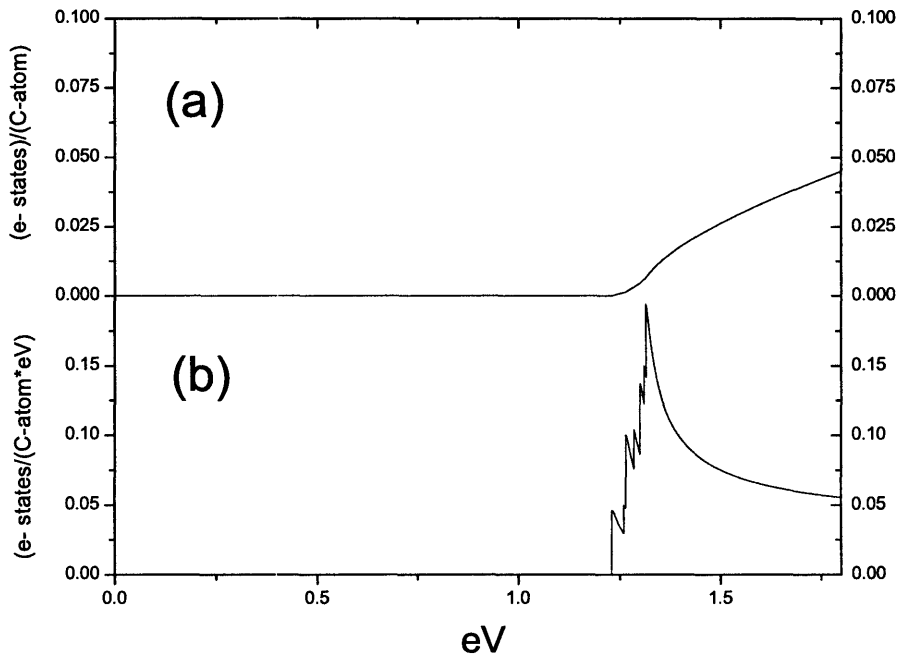

Figure B-19: (b) The total JDOS for all semiconducting SWNTs that would be resonant with E_{Laser}=2.54eV from a diameter distribution of d=1.25±0.20 nm.
(a) The cumulative number of electron states filled or depleted as the JDOS (b) is integrated from 0.0eV to E_{Fermi}.

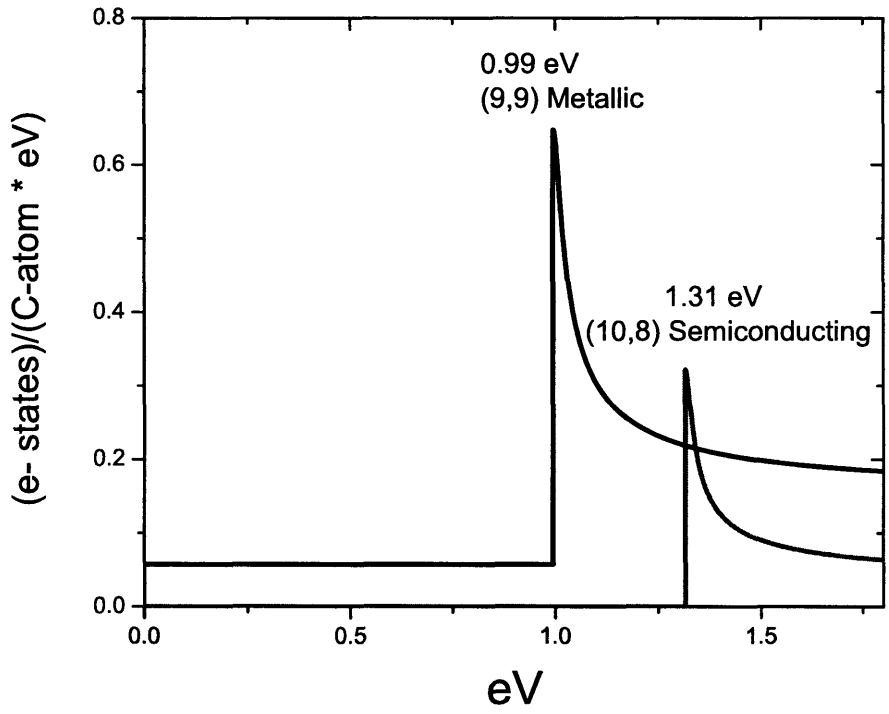

Figure B-20: The E_1 and E_3 van Hove singularities in the JDOS for (9,9) metallic and (10,8) semiconducting SWNTs, respectively.

Bibliography

[1] M. S. Dresselhaus, G. Dresselhaus, and P. Avouris, *Carbon Nanotubes: Synthesis, Structure, Properties and Applications*, volume 80 of *Springer Series in Topics in Appl. Phys.*, Springer-Verlag, Berlin, 2001.

[2] O. Ingan and I. Lundst, Science **284**, 1281 (1999).

[3] J. H. Hafner, C. L. Cheung, and C. M. Lieber, Nature **398**, 761 (1999).

[4] W. A. de Heer et al., Science **268**, 845 (1995).

[5] R. Saito, G. Dresselhaus, and M. S. Dresselhaus, *Physical Properties of Carbon Nanotubes*, Imperial College Press, London, 1998.

[6] G. G. Samsonidze et al., Journal of Nanoscience and Nanotechnology **3**, 431 (2003).

[7] R. Saito, G. Dresselhaus, and M. S. Dresselhaus, Phys. Rev. B **61**, 2981 (2000).

[8] R. Saito et al., Phys. Rev. Lett. **88**, 027401 (2002).

[9] R. Saito et al., New Journal of Physics **5**, 157.1 (2003).

[10] S. D. M. Brown et al., Phys. Rev. B **63**, 155414 (2001).

[11] C. Jiang et al., Phys. Rev. B **66**, 161404 (2002).

[12] A. Jorio et al., Phys. Rev. Lett. **86**, 1118 (2001).

[13] A. Kukovecz, C. Kramberer, V. Georgakilas, M. Prato, and H. Kuzmany, Eur. Phys. J. B **28**, 223 (2002).

[14] R. M. Martin and L. M. Falicov, *Light Scattering in Solids I: edited by M. Cardona*, volume 8, pages 79–145, Springer-Verlag, Berlin, 1983, Chapter 3, Topics in Applied Physics.

[15] C. Thomsen and S. Reich, Phys. Rev. Lett. **85**, 5214 (2000).

[16] J. Kurti, V. Zolyomi, A. Gruneis, and H. Kuzmany, Phys. Rev. B **65**, 165433 (2002).

[17] L. G. Cançado et al., Phys. Rev. B **66**, 035415 (2002).

[18] M. S. Dresselhaus and R. Kalish, *Ion Implantation in Diamond, Graphite and Related Materials*, Springer-Verlag; Springer Series in Materials Science, Berlin, 1992, Volume 22.

[19] A. C. Ferrari and J. Robertson, Phys. Rev. B **64**, 075414 (2001).

[20] M. J. Matthews, M. A. Pimenta, G. Dresselhaus, M. S. Dresselhaus, and M. Endo, Phys. Rev. B **59**, R6585 (1999).

[21] I. Pócsik, M. Hundhausen, M. Koós, and L. Ley, Journal of Non-Crystalline Solids **227-230**, 1083 (1998).

[22] A. C. Ferrari and J. Robertson, Phys. Rev. B **61**, 14095 (2000).

[23] M. S. Dresselhaus, G. Dresselhaus, A. Jorio, A. G. Souza Filho, and R. Saito, Carbon **40**, 2043 (2002).

[24] F. Tuinstra and J. L. Koenig, J. Phys. Chem. **53**, 1126 (1970).

[25] M. S. Dresselhaus and P. C. Eklund, Advances in Physics **49**, 705 (2000).

[26] Y. Wang, D. C. Aolsmeyer, and R. L. McCreery, Chem. Mater. **2**, 557 (1990).

[27] M. A. Pimenta et al., Brazilian J. Phys. **30**, 423 (2000).

[28] Y. Kawashima and G. Katagiri, Phys. Rev. B **52**, 14 (1995).

[29] M. Bonelli, A. Miotello, P. M. Ossi, A. Pessi, and S. Gialanella, Phys. Rev. B **59**, 13513 (1999).

[30] S. D. M. Brown et al., Phys. Rev. B **61**, 7734 (2000).

[31] Y. Kawashima and G. Katagiri, Phys. Rev. B **59**, 62 (1999).

[32] L. Alvarez, A. Righi, S. Rols, E. Anglaret, and J. L. Sauvajol, Chem. Phys. Lett. **320**, 441 (2000).

[33] A. G. Souza Filho et al., Phys. Rev. B **65**, 035404 (2002).

[34] A. G. Souza Filho et al., Phys. Rev. B **65**, 085417 (2002).

[35] J. H. Hafner, C. L. Cheung, T. H. Oosterkamp, and C. M. Lieber, J. Phys. Chem. B **105**, 743 (2001).

[36] Carbon nanotube can be thought as a sheet of graphite rolled up to form a cylinder. The structure is defined by its diameter (d_t) and chiral angle (θ). The d_t and θ nanotube parameters are well represented by the chiral vector $\mathbf{C_h} = n\mathbf{a_1} + m\mathbf{a_2}$ that spans the nanotube circumference and is defined by the two integers (n, m) giving $\mathbf{C_h}$ with respect to the 2D graphite basis vectors $\mathbf{a_1}$ and $\mathbf{a_2}$. These two simple geometric parameters (d_t, θ) or (n, m) are indeed responsible for the large diversity of nanotubes, each (n, m) representing a different molecule with different energy levels and physical properties.

[37] A. Grüneis et al., Phys. Rev. B **65**, 155405 (2002).

[38] R. Saito, T. Takeya, T. Kimura, G. Dresselhaus, and M. S. Dresselhaus, Phys. Rev. B **57**, 4145 (1998).

[39] A. Jorio et al., Phys. Rev. B **65**, 155412 (2002).

[40] M. A. Pimenta et al., Phys. Rev. B **64**, 041401 (2001).

[41] A. Jorio et al., New effects in the resonant Raman features in one-dimensional systems: isolated single wall carbon nanotube studies, in *Proceedings of the*

XV International Winter School on the Electronic Properties of Novel Materials, edited by H. Kuzmany, J. Fink, M. Mehring, and S. Roth, volume 633, pages 285–289, Woodbury, NY, 2002, American Institute of Physics, Kirchberg Winter School, Austria.

[42] A. G. Souza Filho, *Raman in SWNTs*, Ph. D. thesis, Universidade Federal do Ceará, Fortaleza-CE, 60455-760, Brazil, Departamento de Física, 2001.

[43] R. Saito et al., Phys. Rev. B **64**, 085312 (2001).

[44] A. Jorio et al., Phys. Rev. B Rapid **65**, R121402 (2002).

[45] A. Jorio et al., Phys. Rev. B **66**, 115411 (2002).

[46] P. H. Tan, C. Y. Hu, J. Dong, W. C. Shen, and B. F. Zhang, Phys. Rev. B **64**, 214301 (2001).

[47] G. Kern, *Clean and hydrogenated diamond and graphite surfaces*, PhD thesis, Technische Universit at Wien (1998), 1998, Department of Physics.

[48] G. Benedek, . F. Hofman, P. Ruggerone, G. Onida, and L. Miglio, Surf. Sci. Rep. **20**, 1 (1994).

[49] A. S. Pine, G. Dresselhaus, B. J. Palm, R. W. Davies, and S. A. Clough, J. Molec. Spectrosc. **67**, 386 (1977).

[50] G. F. Herzberg, *Infrared and Raman Spectra of Polyatomic Molecules*, Van Nostrand Reinhold, New York, 1949.

[51] V. W. Brar et al., Phys. Rev. B **66**, 155418 (2002).

[52] P. Corio et al., Chem. Phys. Lett. **370**, 675 (2003).

[53] G. U. Sumanasekera et al., Journal of Physical Chemistry B **105**, 10764 (2001).

[54] A. Jorio et al., Phys. Rev. B **63**, 245416 (2001).

[55] R. Saito, A. Gruneis, J. Jiang, and et al, to be published (2004).

[56] Y. Kawashima and G. Katagiri, Phys. Rev. B **52**, 10053 (1995).

[57] P. H. Tan, Y. M. Deng, and Q. Zhao, Phys. Rev. B **58**, 5435 (1998).

[58] Y. Kawashima and G. Katagiri, Phys. Rev. B **59**, 62 (1999).

[59] P. H. Tan et al., Appl. Phys. Letters **75**, 1524 (1999).

[60] R. Saito, M. Fujita, G. Dresselhaus, and M. S. Dresselhaus, Appl. Phys. Lett. **60**, 2204 (1992).